J. Fluid Mech. (2019), *vol.* 859, *pp.* 1057–1083. © Cambridge University Press 2018
doi:10.1017/jfm.2018.858

Turbulent duct flow with polymers

Armin Shahmardi[1], Sagar Zade[1], Mehdi N. Ardekani[1], Rob J. Poole[2], Fredrik Lundell[1], Marco E. Rosti[1,†] and Luca Brandt[1]

[1]Linné Flow Centre and SeRC (Swedish e-Science Research Centre), KTH Mechanics, SE 100 44 Stockholm, Sweden

[2]Department of Engineering, University of Liverpool, Brownlow Street, Liverpool L69 3GH, UK

(Received 22 December 2017; revised 21 September 2018; accepted 19 October 2018; first published online 28 November 2018)

We have performed direct numerical simulation of the turbulent flow of a polymer solution in a square duct, with the FENE-P model used to simulate the presence of polymers. First, a simulation at a fixed moderate Reynolds number is performed and its results compared with those of a Newtonian fluid to understand the mechanism of drag reduction and how the secondary motion, typical of the turbulent flow in non-axisymmetric ducts, is affected by polymer additives. Our study shows that the Prandtl's secondary flow is modified by the polymers: the circulation of the streamwise main vortices increases and the location of the maximum vorticity moves towards the centre of the duct. In-plane fluctuations are reduced while the streamwise ones are enhanced in the centre of the duct and dumped in the corners due to a substantial modification of the quasi-streamwise vortices and the associated near-wall low- and high-speed streaks; these grow in size and depart from the walls, their streamwise coherence increasing. Finally, we investigated the effect of the parameters defining the viscoelastic behaviour of the flow and found that the Weissenberg number strongly influences the flow, with the cross-stream vortical structures growing in size and the in-plane velocity fluctuations reducing for increasing flow elasticity.

Key words: drag reduction, polymers, turbulence simulation

1. Introduction

1.1. *Aims and objectives*

Near-wall turbulence is responsible for significant drag penalties in many flows of engineering relevance, and because of that, many researchers are studying various ways to be able to properly control the flow (Choi, Moin & Kim 1993; Dubief *et al.* 2004; Breugem, Boersma & Uittenbogaard 2006; Orlandi & Leonardi 2008; García-Mayoral & Jiménez 2011; Rosti, Cortelezzi & Quadrio 2015; Rosti, Brandt & Pinelli 2018*b*). Among the many control strategies, the use of polymers has been demonstrated to be very efficient to reduce drag in pipelines (Virk 1971). While flows through axisymmetric geometry have been extensively studied (Virk *et al.* 1967; Cho & Harnett 1982; Den Toonder *et al.* 1997; Escudier, Presti & Smith 1999; Ptasinski *et al.* 2003; Resende *et al.* 2006), less attention has been given to more complex

† Email address for correspondence: merosti@mech.kth.se

https://doi.org/10.1017/jfm.2018.858 Published online by Cambridge University Press

geometries, such as square ducts. In this context, the aim of this work is to explore and better understand the interactions between the turbulent flow in ducts with square section and polymer additives.

1.2. *Duct flow*

Turbulent flow in a plane channel has been extensively studied in the past (Kim, Moin & Moser 1987), while the flow in a duct with a square cross-section has received much less attention (Uhlmann *et al.* 2007; Pinelli *et al.* 2010; Samanta *et al.* 2015; Vinuesa, Schlatter & Nagib 2015; Owolabi, Poole & Dennis 2016), although its geometry is only mildly more complex. Peculiar features of the turbulent flow in a duct are that the mean velocity profile presents a non-uniform distribution of the skin friction coefficient along the edges, and the related appearance in the cross-sectional plane of secondary motions of the second kind, as classified by Prandtl (1926), which is a mean flow effect induced by gradients of turbulence fluctuations, e.g. a breaking of axisymmetry. The existence of such secondary mean motion in this geometrical configuration has been well known since the experiments by Nikuradse (1926), which were followed by further experimental measurements (Brundrett & Baines 1964; Gessner 1973; Melling & Whitelaw 1976) as well as direct numerical and large-eddy simulations (Madabhushi & Vanka 1991; Gavrilakis 1992; Uhlmann *et al.* 2007; Pinelli *et al.* 2010), all of which subsequently extended our knowledge of this flow. Uhlmann *et al.* (2007) simulated the case of the marginal Reynolds-number regime and showed that the buffer-layer coherent structures play a crucial role in the appearance of the secondary flow and in the deformation of the mean streamwise velocity profile. Indeed, they proposed that the deformation of the mean streamwise velocity profile is due to the presence of preferential positions of quasi-streamwise vortices and velocity streaks. Moreover, in such a marginal regime, short-time-averaged velocity fields are found to exhibit a four-vortex state instead of the usual eight-vortex secondary flow pattern found at higher Reynolds numbers. This feature was explained with the relation between coherent structures and secondary flow: if the dimension of the cross-section, in wall units, is below that needed to accommodate a complete minimal turbulent cycle on all four walls (Jimenez & Moin 1991), then just two facing walls can alternately give rise to a complete turbulent regeneration mechanism, while the other two faces remain in a relative quiescent state. Such four-vortex states at marginal Reynolds number have also been observed experimentally (Owolabi *et al.* 2016). Pinelli *et al.* (2010) studied turbulent duct flows at higher Reynolds numbers, where the length of the edge of the square cross-section, expressed in viscous units, is larger, therefore allowing for the simultaneous presence of multiple pairs of high- and low-velocity streaks. These authors further proved the idea that the secondary flow is a footprint of the coherent motions embedded in the turbulent flow, and proposed a scenario in which the position of the centre of the mean secondary vortices is determined by the preferential positioning of the quasi-streamwise vortices.

1.3. *Polymer additives*

Polymer addition is a very efficient strategy employed for drag reduction in wall-bounded turbulent flows, since drag reduction up to 80 % has been achieved with concentrations of only a few parts per million. Two distinct regimes are usually identified (Warholic, Massah & Hanratty 1999), often called low and high drag reduction (LDR and HDR, respectively). The former (LDR) exhibits a log-law region

https://doi.org/10.1017/jfm.2018.858 Published online by Cambridge University Press

of the mean velocity profile parallel to that of the Newtonian flow, but with an upward shift associated with the amount of drag reduction; streamwise fluctuations are increased while wall-normal and spanwise components are reduced, as well as the shear stress. The regime characterised by high drag reductions (HDR), more than 40 %, shows a strong increase in the slope of the log-law region and low levels of Reynolds shear stress (Ptasinski *et al.* 2003). The drag reduction is eventually bounded by a maximum drag reduction (MDR) (Virk, Mickley & Smith 1970). Several works (Warholic *et al.* 1999; Ptasinski *et al.* 2003) observed low-Reynolds shear stress and a consequent deficit in the stress balance equation, which has been interpreted as the input of energy from the polymers to the flow which ultimately sustains the asymptotic MDR.

The drag reduction mechanism is quite complex due to its multiscale nature (a small amount of microscopic polymer molecules is needed to achieve significant drag reduction in the bulk flow) and its full physical understanding is still incomplete. Several explanations have been proposed to gain further insight into the mechanism of polymer drag reduction: Dimitropoulos *et al.* (2001) showed that streamwise enstrophy is inhibited by the extensional viscosity generated by polymers stretched by turbulence; Ptasinski *et al.* (2003) found a shear sheltering effect in the near-wall region which decouples the outer- and inner-layer vortices; Min, Choi & Yoo (2003*a*) and Min *et al.* (2003*b*) observed the transport of elastic energy from the viscous sublayer to the buffer and the log region, and proposed a criterion for the onset of drag reduction.

Dubief *et al.* (2004, 2005) studied the intermittency of polymers in turbulent flows, showing that the action of polymers is as intermittent as the near-wall vortices, and that the drag-reducing property of polymers is closely related to coherent turbulent structures. Polymers dampen near-wall vortices but also enhance streamwise kinetic energy in near-wall streaks. The net balance of these two opposite actions leads to a self-sustained drag-reduced turbulent flow: the polymers reduce turbulence by opposing the downwash and upwash flows generated by near-wall vortices, while they enhance streamwise velocity fluctuations in the very near-wall region. Recent studies by Xi & Graham (2010, 2012*a*,*b*) provided new insight into the mechanism by which polymer additives reduce the drag. These authors suggested that a turbulent flow is characterised by an alternate succession of strong and weak turbulence phases. The first are characterised by flow structures showing strong vortices and wavy streaks, the latter by weak streamwise vortices and almost streamwise-invariant streaks. In the Newtonian flow, the so-called active turbulence dominates; with increasing viscoelasticity, on the contrary, active intervals becomes shorter while the so-called hibernating intervals are unaffected. Also, it is shown that during these hibernating turbulence intervals, the turbulent dynamics resemble MDR turbulence in both Newtonian and viscoelastic flows (White, Somandepalli & Mungal 2004; Li, Sureshkumar & Khomami 2006).

Polymers can also alter flow instabilities and transition to turbulence. Indeed, Biancofiore, Brandt & Zaki (2017) recently examined the secondary instability of streaks in a viscoelastic flow, showing that the streaks reach a lower average energy with increasing elasticity due to a resistive polymer torque that opposes the streamwise vorticity and, as a result, opposes the lift-up mechanism.

1.4. *Polymer solutions in square duct flows*

Extensive work has been done experimentally to try to characterise polymer solution behaviour in duct flows. In particular, Logan (1972) and Rudd (1972) reported limited

https://doi.org/10.1017/jfm.2018.858 Published online by Cambridge University Press

measurements of the mean-flow and turbulence structure for flow of drag-reducing polymers through square tubes, with sufficiently low polymer concentrations, and provided no information about the secondary flow. More recently, Gampert & Rensch (1996) have reported the results of a systematic study of the influence of polymer concentration on near-wall turbulence structure for the flow through a square duct, but again have provided no direct information on the secondary flow. Also, they argued that there are two flow regimes in which the properties of the polymer structure, and hence the turbulent flow field, differ significantly, depending on the polymer concentration. Escudier & Smith (2001) presented both global data (friction factor versus Reynolds number) and detailed mean axial and secondary flow velocity and turbulence field data for fully developed flow through a square duct of various polymer solutions. They found a reduction in the intensity of turbulent velocity fluctuations transverse to the mean flow and a strong reduction in the secondary flow velocities. More recently, Escudier, Nickson & Poole (2009) provided a comprehensive database of previous experimental works (Rudd 1972; Gampert & Yong 1990; Escudier & Smith 2001; Gampert *et al.* 2005); the authors pointed out that several of these studies have limited turbulence data, and consider mainly relatively low polymer concentrations. Escudier *et al.* (2009) placed special emphasis on the quantification of turbulence anisotropy and showed that, with polymer additives, the flow displays a tendency towards the axisymmetric turbulence limit. Also, there is a marked decrease in anisotropy with distance from the near-surface peak in all cases, but this tendency progressively reduces with increasing concentration/drag-reduction level. Recently, Owolabi, Dennis & Poole (2017) have explored the relationship between drag reduction and fluid elasticity, and describe a technique for an *a priori* quantitative prediction of drag reduction from a knowledge of polymer relaxation time, flow rate and geometric length scale, based on a universal relationship between drag reduction and fluid elasticity. Although the previous discussion suggests a satisfactory situation from an engineering viewpoint, for polymer solutions a full understanding of the phenomena is still missing.

1.5. *Outline*

In this work, we present direct numerical simulations (DNS) of a turbulent duct flow with polymer additives at moderate Reynolds number. In the simulations, the viscoelastic fluid is modelled by the constitutive FENE-P (finite extensible nonlinear elasticity–Peterlin) closure. In § 2, we first discuss the flow configuration and governing equations, and then present the numerical methodology used. The features of the turbulent duct flow are documented in § 3, where we compare results with and without the polymer additives, to elucidate their effect on the secondary motion and on the flow in general at this moderate Reynolds number. First- and second-order statistics are analysed, together with energy and vorticity budgets. Finally, a summary of the main findings and some conclusions are drawn in § 4.

2. Formulation

We consider the turbulent flow of an incompressible viscoelastic fluid through a square duct. Figure 1 shows a sketch of the geometry and the Cartesian coordinate system, where x, y and z (x_1, x_2 and x_3) denote the streamwise, and the two cross-stream coordinates, while u, v and w (u_1, u_2 and u_3) denote the respective components of the velocity vector field. The lower and upper walls are located at $y = \pm h$, while the left and right walls are at $z = \pm h$, where h is the cross-section half-size. Moreover, we

https://doi.org/10.1017/jfm.2018.858 Published online by Cambridge University Press

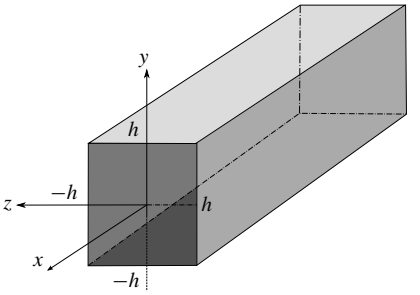


FIGURE 1. Sketch of the square duct geometry and coordinate system adopted with the walls located at $y=-h$ and $y=h$, and at $z=-h$ and $z=h$.

define $\widetilde{y}$ as the distance from the wall. The Reynolds number of the flow is defined as $Re=U_b h/\nu$, where h is chosen as characteristic length scale, the characteristic velocity is the bulk velocity U_b, defined as the average value of the mean velocity computed across the whole domain, and ν is the total kinematic viscosity, i.e. the sum of the solvent and polymer viscosity. Hereafter, all the velocity components will be made non-dimensional with U_b and lengths with h, except where explicitly stated otherwise.

The fluid is governed by the incompressible Navier–Stokes equations:

$$\frac{\partial u_i}{\partial t}+\frac{\partial u_i u_j}{\partial x_j}=-\frac{\partial p}{\partial x_i}+\frac{\beta}{Re}\frac{\partial^2 u_i}{\partial x_j \partial x_j}+\frac{1-\beta}{Re}\frac{\partial \tau_{ij}}{\partial x_j}, \tag{2.1a}$$

$$\frac{\partial u_i}{\partial x_i}=0, \tag{2.1b}$$

where p is the pressure, β the ratio of the solvent viscosity to the total fluid viscosity, and τ_{ij} the extra stress tensor due to the polymers. Note that if β equals 1, the standard Navier–Stokes equations are recovered. To model the additional stresses due to the presence of polymers in the flow, we use the FENE-P closure where the polymer stress tensor τ_{ij} is written as a function of the configuration tensor C_{ij} as

$$\tau_{ij}=\frac{1}{Wi}\left(\frac{C_{ij}}{1-\dfrac{C_{kk}}{L^2}}-\delta_{ij}\right). \tag{2.2}$$

In the expression above, L is the dumbbell extensibility, C_{kk} the trace of the configuration tensor, and Wi the Weissenberg number defined as the ratio between the elastic and viscous forces (Dealy 2010; Poole 2012), i.e. $Wi=\lambda U_b/h$ with λ being the polymer relaxation time and δ_{ij} the Kronecker delta. The configuration tensor is a symmetric second-order tensor, which is found by solving the following dynamic equation:

$$\frac{\partial C_{ij}}{\partial t}+u_k\frac{\partial C_{ij}}{\partial x_k}=C_{kj}\frac{\partial u_i}{\partial x_k}+C_{ik}\frac{\partial u_j}{\partial x_k}-\tau_{ij}. \tag{2.3}$$

The equation is a balance between the advection of the configuration tensor on the left-hand side, and the stretching and relaxation of the polymer, represented by the first two terms and the last one on the right-hand side, respectively.

https://doi.org/10.1017/jfm.2018.858 Published online by Cambridge University Press

2.1. *Numerical implementation*

The code for the numerical solution of the equations above is an extension of that described by Rosti & Brandt (2017, 2018) and Rosti, Brandt & Mitra (2018*a*), with which it shares its general architecture. The time integration method used to solve the equations is based on an explicit fractional-step method (Kim & Moin 1985), where all the terms are advanced with the third-order Runge–Kutta scheme, except the viscous stress contribution, which is advanced with Crank–Nicolson (Min, Yoo & Choi 2001). In particular, to solve the system of governing equations, at every time step, we perform the following steps (see also Min *et al.* 2001; Dubief *et al.* 2005): (i) the updated conformation tensor C_{ij} is found by solving (2.3) with the last term τ_{ij} substituted by (2.2); (ii) the polymer stress tensor τ_{ij} is computed by (2.2); and (iii) the Navier–Stokes equations (2.1) are advanced in time first by solving the momentum equation (prediction step), then by solving a Poisson equation for the projection variable, and finally by correcting the velocity and pressure to make the velocity field divergence free (correction step).

The numerical solution of (2.3) is cumbersome, and many researchers have shown that the numerical solution of a viscoelastic fluid is unstable, especially in the case of high Weissenberg numbers, since any disturbance amplifies over time (Dupret & Marchal 1986; Sureshkumar & Beris 1995; Min *et al.* 2001). Indeed, equation (2.3) can easily diverge and lead to the numerical breakdown of the solution since it is an advection equation without any diffusion term (Dubief *et al.* 2005). One of the earliest solutions to this problem was to introduce an artificial diffusivity (AD) to the constitutive equations (Sureshkumar & Beris 1995; Mompean & Deville 1997; Alves, Pinho & Oliveira 2000). Subsequently, global AD was replaced by local AD, a method that has been widely used. In the present work, we use global AD in the first transient part of the simulation of a viscoelastic flow, and then gradually remove it while approaching the final statistical steady-state regime, when it is completely removed. Also, we chose to use a fifth-order weighted essentially non-oscillatory (WENO) scheme (Jiang & Shu 1996) for the advection terms in (2.3). Apart from that, the governing differential equations are solved on a staggered grid using a second-order central finite-difference scheme. This methodology has been proved to work properly by Sugiyama *et al.* (2011) and also successfully used by Rosti & Brandt (2017) for viscoelastic solid-like materials. A comprehensive review on the properties of different numerical schemes for the advection term is reported by Min *et al.* (2001).

2.2. *Numerical details*

For all the turbulent flows considered hereafter, the equations of motion are discretised by using $448 \times 448 \times 448$ grid points on a computational domain of $12h \times 2h \times 2h$ in the streamwise, wall-normal and spanwise directions, respectively. The spatial resolution has been chosen in order to properly resolve the wall turbulence, satisfying the constraint $\Delta y^+ = \Delta z^+ \approx 0.8$ and $\Delta x^+ \approx 5$ in the Newtonian case.

Viscous units, used above to express spatial resolution, will often be employed in the following; they are indicated by the superscript $^+$, and are built using the friction velocity u_τ as velocity scale and the viscous length $\delta_\nu = \nu/u_\tau$ as length scale. For a turbulent Newtonian duct flow, the friction velocity is defined as

$$u_\tau = \sqrt{\nu \frac{\partial u^*}{\partial y^*}}, \tag{2.4}$$

https://doi.org/10.1017/jfm.2018.858 Published online by Cambridge University Press

where ν is the kinematic viscosity, u^* and y^* denote the dimensional values of velocity and distance from the wall, and the derivative is taken at the wall (note that the equation is written for the top and bottom walls, but a similar one can be written for the left and right walls by changing y to z). When the flow is viscoelastic, the definition (2.4) must be modified to account for the polymeric stress, which is in general non-zero at the wall. Thus, we define

$$u_\tau = \sqrt{\beta\nu\frac{\mathrm{d}u^*}{\mathrm{d}\tilde{y}^*} + \left(\frac{1-\beta}{\rho}\right)\tau_{12}{}^*}, \tag{2.5}$$

with $\tau_{12}{}^*$ being the dimensional polymeric stress. All the simulations are performed at constant flow rate consistent with choosing U_b as the characteristic velocity; the flow Reynolds number based on the bulk velocity is fixed at 2800, i.e. $Re = U_b h/\nu = 2800$, where the bulk velocity is the average value of the mean velocity computed across the whole domain occupied by the fluid phase. This choice facilitates the comparison between the Newtonian and viscoelastic flows. Since we are enforcing the constant-flow-rate condition, the appropriate instantaneous value of the streamwise pressure gradient is determined at every time step.

All the simulations are started from a fully developed turbulent duct flow without polymer additives. After the flow has reached statistical steady state, the calculations are continued for an interval of $400h/U_b$ time units, during which 400 full flow fields are stored for further statistical analysis. To verify the convergence of the statistics, we have computed them using different numbers of samples and verified that the differences are negligible.

2.3. *Code validation*

The code has been extensively validated in the past for turbulent flow simulations (Rosti & Brandt 2017). Here, we provide one more comparison with literature results for the case of a turbulent duct flow. We compare our results of a Newtonian turbulent duct flow at $Re = 2800$ with those reported by Uhlmann *et al.* (2007) and Pinelli *et al.* (2010) at a slightly higher Reynolds number, $Re = 2900$. Figure 2(*a–c*) shows the mean velocity profile in logarithmic scale and figure 2(*d–f*) shows the cross-term of the Reynolds stress tensor $u'v'$ as a function of the distance from the wall, $\tilde{y}$. Three different sections are considered: the centreline $z = 0$, and $z = 0.3h$ and $z = 0.6h$. Overall good agreement between the literature (shown with the black dots) and our results (shown with the blue solid line) is evident.

The FENE-P model implementation has been validated by simulating a viscoelastic temporally evolving mixing layer flow and by comparing our results with those provided by Min *et al.* (2001). We consider an initial velocity field defined as $u = 0.5\tanh y$, and trigger the roll-up of the shear layer with a small two-dimensional perturbation. The characteristic velocity and length scales are $\Delta u = u_{max} - u_{min}$ and $\delta = \Delta u/(\mathrm{d}u/\mathrm{d}y)_{max}$, respectively. The Reynolds number is fixed at $Re = \delta\Delta u/\nu = 50$ (ν being the total kinematic viscosity) and the Weissenberg number $Wi = \lambda\Delta u/\delta = 25$; moreover, the extensibility L^2 is set to 100, and the ratio of polymeric and solvent viscosity is set to 0.1. The two-dimensional numerical domain has size $30\delta \times 100\delta$, discretised by 128×384 grid points. Note that the flow configuration and domain are the same as used by Min *et al.* (2001). Figure 3(*a–c*) shows instantaneous vorticity contours for the flow, where we can observe that the initial perturbation grows in time and generates two vortices (panel (*a*), $t \approx 20\delta/\Delta u$), which roll up (panel (*b*), $t \approx 60\delta/\Delta u$) and eventually merge into one large vortex (panel (*c*), $t \approx 100\delta/\Delta u$).

https://doi.org/10.1017/jfm.2018.858 Published online by Cambridge University Press

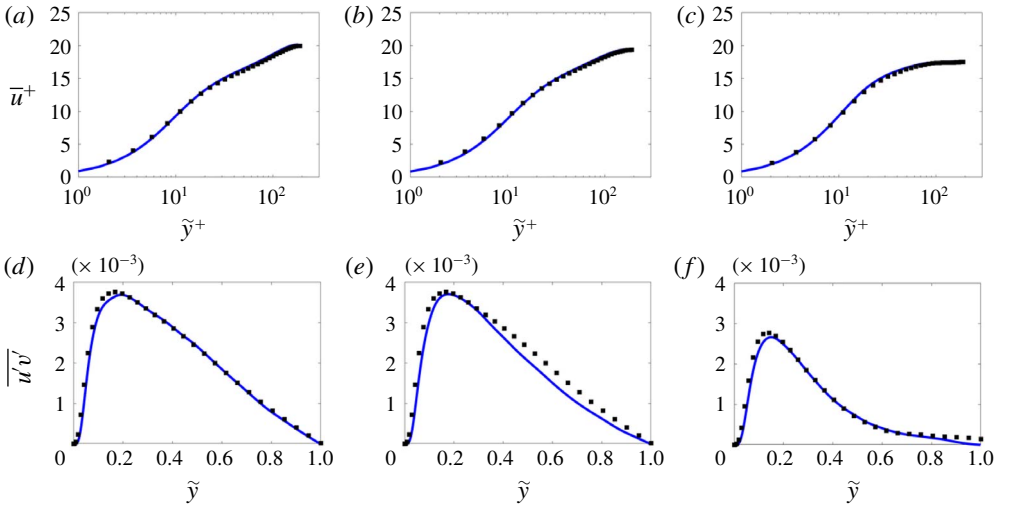


FIGURE 2. (Colour online) (*a–c*) Mean streamwise velocity component u as a function of the wall-normal distance, indicated with $\tilde{y}$, for the case of a Newtonian turbulent duct flow. (*d–f*) Mean $u'v'$ component of the Reynolds stress tensor profile in bulk units. Panels (*a*,*d*), (*b*,*e*) and (*c*,*f*) correspond to the sections $z = 0$, $0.3h$ and $0.6h$, respectively. Blue solid lines are used for our numerical results, while the black dots are the results from Uhlmann *et al.* (2007) and Pinelli *et al.* (2010).

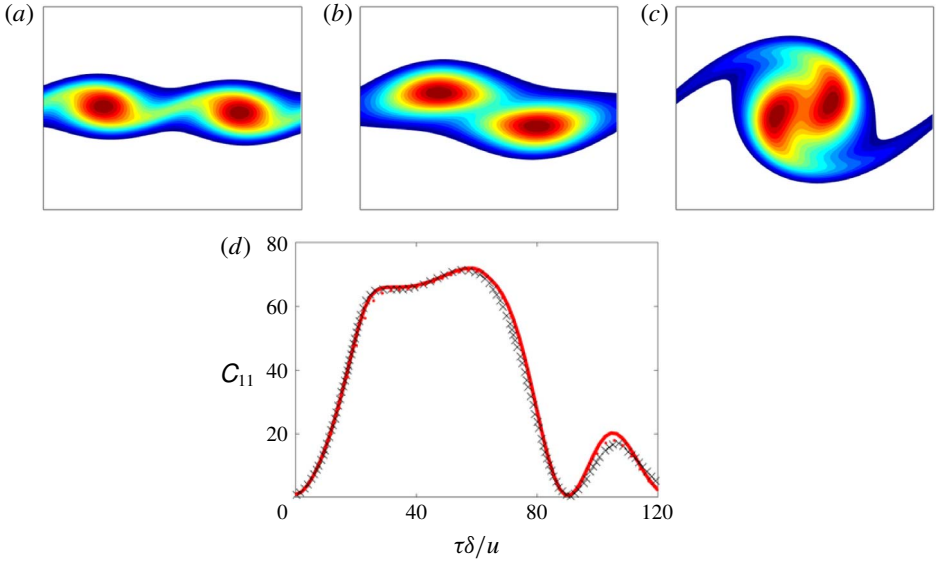


FIGURE 3. (Colour online) (*a–c*) Instantaneous contours of the absolute value of vorticity at times $t \approx 20\delta/\Delta u$, $60\delta/\Delta u$ and $100\delta/\Delta u$, respectively. The colour scale from blue to red ranges from 0.05 to 0.4 in (*a*), from 0.05 to 0.3 in (*b*) and from 0.05 to 0.25 in (*c*). (*d*) Time evolution of the C_{11} component of the polymer conformation tensor. The solid red line displays our numerical results, while the crosses are those by Min *et al.* (2001).

https://doi.org/10.1017/jfm.2018.858 Published online by Cambridge University Press

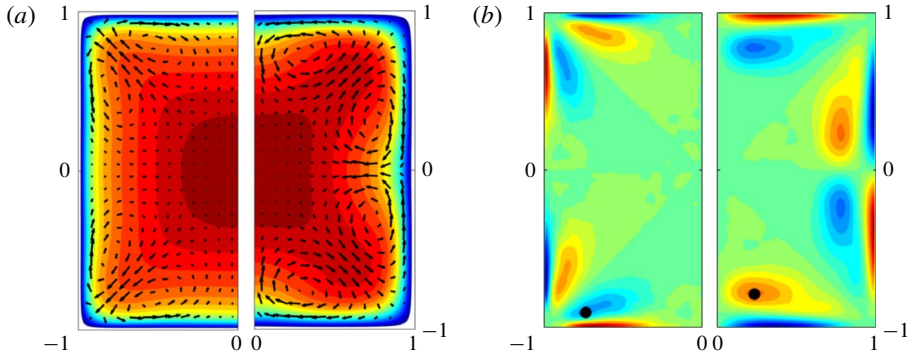


FIGURE 4. (Colour online) Contours of the mean streamwise component of (*a*) velocity $\overline{u}$ and (*b*) vorticity $\overline{\omega}_x$. In each panel, the left (right) half of the duct is used for the Newtonian (viscoelastic) fluid, respectively. The colour scale ranges from 0 (blue) to $1.4U_b$ (red) in (*a*), and from $-0.5U_b/h$ (blue) to $0.5U_b/h$ (red) in (*b*). Panel (*a*) also reports the in-plane mean velocity with arrows.

The quantitative validation is shown in figure 3(*d*), where we plot the time history of C_{xx} in the centre of the domain: crosses are used for the literature results, whereas the red solid line indicates our numerical data. As shown by Min *et al.* (2001), different numerical schemes provide slightly different amplitudes of the maxima of C_{11}, with lower values for highly dissipating schemes or with the inclusion of artificial numerical dissipation; in our simulation, we use the high-order WENO scheme for the advection of the conformation tensor and neglect any artificial dissipation, and we find good agreement of the deformation time history over the whole vortex merging process (Rosti & Brandt 2017; De Vita *et al.* 2018; Izbassarov *et al.* 2018; Rosti *et al.* 2018*c*).

3. Results

We study turbulent duct flows with polymers and start our analysis by considering two cases at $Re = 2800$ (based on the bulk velocity U_b, duct half-height h and total kinematic viscosity ν), Newtonian fluid and viscoelastic fluid consisting of a suspension of polymers as introduced in the previous section. The chosen polymer solution is characterised by the following parameters: $\beta = 0.9$, $L^2 = 3600$ and $Wi = 1.5$ ($Wi_{\tau_0} = \lambda u_{\tau_0}^2/\nu = 18$, with u_{τ_0} being the friction velocity of the Newtonian simulation). Using the previous set of parameters, the Newtonian case has an average friction Reynolds number Re_τ equal to 183, while the polymer one provides a value of 155, which corresponds to a drag reduction DR of approximately 29 %, computed as $DR = -\Delta\tau_w/\tau_{w0}$, where $\Delta\tau_w = \tau_w - \tau_{w0}$, with τ_w being the total shear stress at the wall (as in the computation of the friction velocity), averaged over all four sides, and τ_{w0} the value for the Newtonian case. The Newtonian results will be represented hereafter in blue and the polymer ones in red.

3.1. *Flow statistics*

Figure 4 shows the contours of (*a*) the mean streamwise velocity component $\overline{u}$ and (*b*) the mean streamwise vorticity component $\overline{\omega}_x$, where, in each panel, the left half of the duct reports the data for the Newtonian flow, whereas the right half is for the

https://doi.org/10.1017/jfm.2018.858 Published online by Cambridge University Press

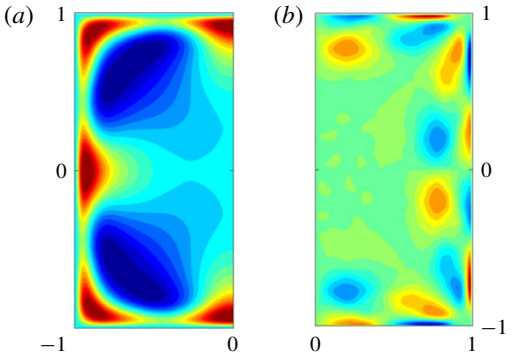


FIGURE 5. (Colour online) Contours of the difference of the mean streamwise component of (*a*) the velocity $\overline{u}$ and (*b*) the vorticity $\overline{\omega}_x$ between the Newtonian and viscoelastic fluids. The colour scale ranges from -0.2 (blue) to $0.2U_b$ (red) in (*a*) and from $-0.5U_b/h$ (blue) to $0.5U_b/h$ (red) in (*b*).

viscoelastic counterpart. For more clarity, figure 5 shows the difference between the Newtonian and viscoelastic flows. The Newtonian case shows the streamwise velocity contour typical of a duct flow, characterised by the symmetry inherited from the considered geometry. The maximum streamwise velocity is located at the centre of the duct and equals $1.3U_b$. The streamwise vorticity displays the in-plane secondary flow typical of turbulent duct flows: eight regions (four in the half-section shown) can be easily identified with alternate sign of vorticity, located symmetrically with respect to the horizontal and vertical lines passing through the centre and with the two diagonals. In particular, in figure 4 we mark with a filled black circle the location of one of the maxima of the vorticity, which we find at $y = -0.74h$, $z = -0.9h$ in the Newtonian case. In the polymeric flows, the streamwise velocity and vorticity components are altered (see figure 5): indeed, the two flows differ mainly in the near-wall region, with strong differences in the streamwise velocity close to the corners. The difference in the streamwise vorticity component is mostly concentrated along the edges. In particular, the streamwise velocity contour exhibits higher values close to the corners and, at the same time, the secondary flow is modified, with the locations of the maximum vorticity moving towards the centre, i.e. they are displaced away from the walls. In fact, the coordinates of the selected maximum vorticity become $y = 0.23h$, $z = 0.78h$. The magnitude of the vorticity maxima are also modified, reducing by 20 % from $0.29U_b/h$ in the Newtonian fluid to $0.23U_b/h$ in the presence of polymers, while the overall integral of the vorticity in each of the eight sectors increases by 17 % from $0.023U_b/h$ in the Newtonian flow to $0.027U_b/h$ in the viscoelastic one. Thus, although the peak value of the in-plane vorticity is reduced, overall it is enhanced by the polymer addition due to an enlargement of the area with non-zero vorticity. The modification of the secondary flow is further analysed by the maximum of the magnitude of $\overline{v}$ in the domain; indeed, this slightly decreases from approximately $0.019U_b$ in the Newtonian flow to $0.018U_b$ in the polymer solution.

Figure 6 shows the mean streamwise velocity component $\overline{u}$ as a function of the wall-normal distance $\widetilde{y}$ (both in wall units). Figure 6 shows (*a*) the mean velocity profile in the midplane ($z = 0$), (*b*) the velocity at $z = 0.3h$ and (*c*) the velocity at $z = 0.6h$. In the midplane, where the secondary flow is weak, we can identify three regions in

https://doi.org/10.1017/jfm.2018.858 Published online by Cambridge University Press

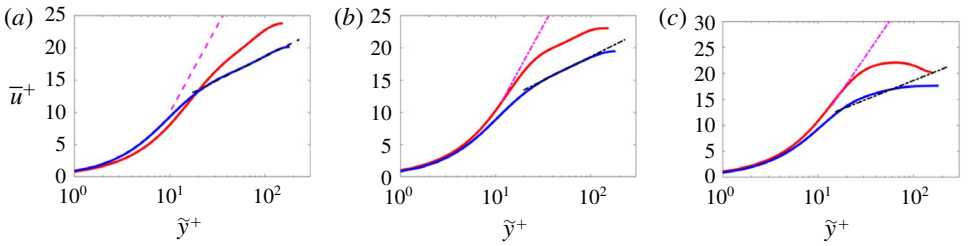


FIGURE 6. (Colour online) Mean streamwise velocity as a function of the wall-normal distance in logarithmic scale and wall units. The blue and red lines are used for the numerical results without and with polymers. The magenta dashed line is the polymer maximum drag reduction (Virk 1975; Lvov *et al.* 2004) while the black dashed line is the Newtonian log law. The panels correspond to different sections: (*a*) $z=0$, (*b*) $z=0.3h$ and (*c*) $z=0.6h$.

the velocity profile of the Newtonian fluid (figure 6*a*) similarly to what is found for a turbulent channel flow: first, the viscous sublayer for $\widetilde{y}^+ < 5$ where the variation of $\overline{u}^+$ with $\widetilde{y}^+$ is approximately linear; then, the so-called log-law region, $\widetilde{y}^+ > 30$, where the variation of $\overline{u}^+$ versus $\widetilde{y}^+$ is logarithmic; finally, the region between 5 and 30 wall units is called the buffer layer and neither laws hold. As we approach the sidewalls, $x = 0.3h$ and $0.6h$, the range of the equilibrium layer where the velocity profile is logarithmic reduces (figure 6*b*), eventually disappearing (figure 6*c*). The profiles have similar trends for the viscoelastic fluid, in which case, however, the inertial range has an upward shift, consistent with the observed drag reduction (Warholic *et al.* 1999). Note that all the data stay below the MDR curve (Virk 1975; Lvov *et al.* 2004), a limit curve approached only in the case of very high *Wi*, shown as the magenta dashed line in figure 6.

Figure 7 displays the velocity fluctuation profile as a function of the wall-normal distance $\widetilde{y}$. In particular, figure 7(*a–c*) reports the root mean square (r.m.s.) of the streamwise component of the velocity fluctuations u_{rms}, figure 7(*d–f*) shows the r.m.s. of one of the wall-normal components v_{rms}, and figure 7(*g–i*) displays the cross-term of the Reynolds stress tensor, $u'v'$. The Newtonian case shows a peak of u_{rms} close to the wall, with slightly different values in the three sections, decreasing when moving from the midplane towards the sidewalls. Away from the wall, the streamwise velocity fluctuations reach a plateau with a local minimum whose amplitude is approximately half the peak value in the centreline. On the other hand, the wall-normal velocity fluctuations have a weak maximum close to the wall in the centreline, which then decreases at $z = 0.3h$, and eventually disappears at $z = 0.6h$, when approaching the corners. The flow with polymers displays similar r.m.s. profiles; however, the peaks of both u_{rms} and v_{rms} are located further away from the wall; also, a strong decrease in the wall-normal fluctuation v_{rms} is observed in all sections, whereas an increase in the streamwise component is evident only close to the centreline, as observed in-plane channels. Finally, we consider the cross-term of the Reynolds stress tensor $u'v'$; the profiles show a peak close to the wall and a value approaching zero towards the centreline due to symmetry. The profile at $z = 0.3h$ has a lower peak, and still decreases monotonically after its maximum value; on the other hand, the Reynolds stress $u'v'$ closer to the sidewalls, $z = 0.6h$, goes to zero rapidly and remains approximately zero until $\tilde{y} = h$. In the cases with polymers, the Reynolds shear stress is much weaker than in the Newtonian cases; it even becomes negative

https://doi.org/10.1017/jfm.2018.858 Published online by Cambridge University Press

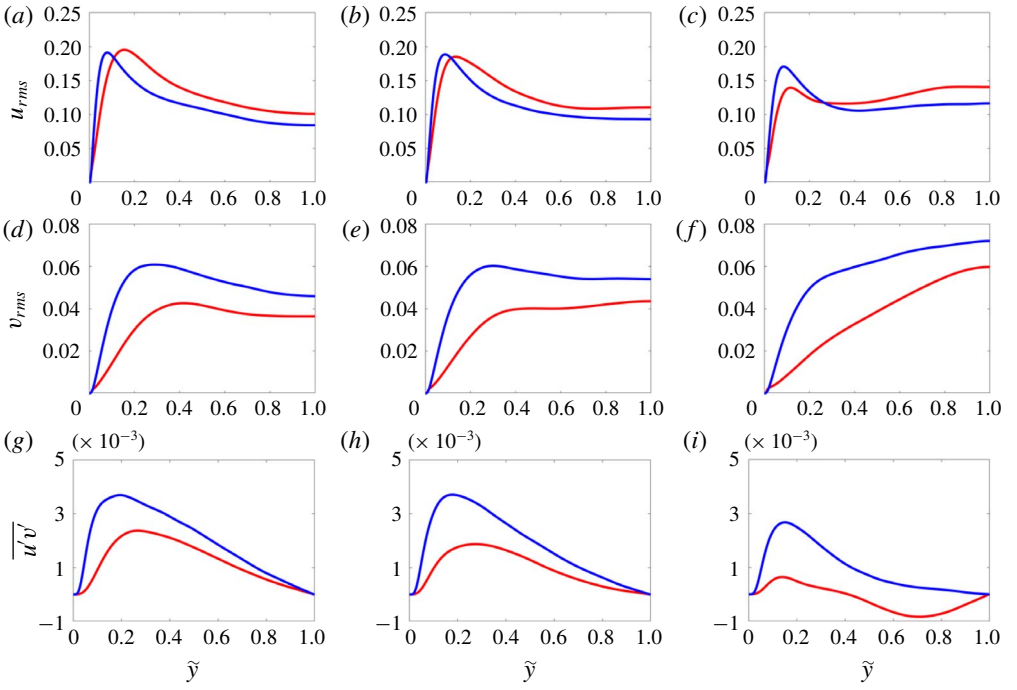


FIGURE 7. (Colour online) Wall-normal mean profile of (*a–c*) the streamwise r.m.s. velocity fluctuation, (*d–f*) the wall-normal r.m.s. velocity fluctuation, and (*g–i*) the cross-term of the Reynolds stress tensor $u'v'$. The columns correspond to different sections: (*a*,*d*,*g*) $z = 0$, (*b*,*e*,*h*) $z = 0.3h$ and (*c*,*f*,*i*) $z = 0.6h$. The line and colour style is the same as in figure 6.

away from the wall in the section at $z = 0.6h$. This is due to the transverse shear near the walls leading to additional vorticity (figure 4); this effect is more pronounced in the viscoelastic case than in the Newtonian flow, due to the enhancement of the near-wall vorticity, as shown in figure 5(*b*). Overall, the velocity fluctuation data indicate that the polymer solution has enhanced streamwise velocity fluctuations, and strongly reduced in-plane components and shear stresses, in good agreement with many previous studies in the literature (see e.g. the collection of data from numerous authors in Escudier *et al.* (2009)).

We conclude the analysis of the main flow statistics by showing in figure 8 four components of the conformation tensor C_{ij}. Note that the conformation tensor is strongly related to the added stress term due to the polymers (see (2.2)). In particular, in figure 8 we show the streamwise diagonal component C_{11}, one of the two diagonal in-plane components C_{22}, the corresponding off-diagonal term C_{12}, and the in-plane off-diagonal term C_{23}. The other components can be deduced from symmetry arguments: in particular, C_{33} and C_{13} can be obtained from C_{22} and C_{12} by symmetry around the bisection of the quadrants I and III. As expected, the streamwise component is the dominant one, with strong peak values located close to the wall, while, interestingly, in the four corners and in the centre of the duct C_{11} reaches its minimum value. Also, C_{11} is the only diagonal component of the conformation tensor showing the full eight symmetries; indeed, C_{22} presents only horizontal and vertical symmetries, with the diagonal ones recovered through the combination with the other

https://doi.org/10.1017/jfm.2018.858 Published online by Cambridge University Press

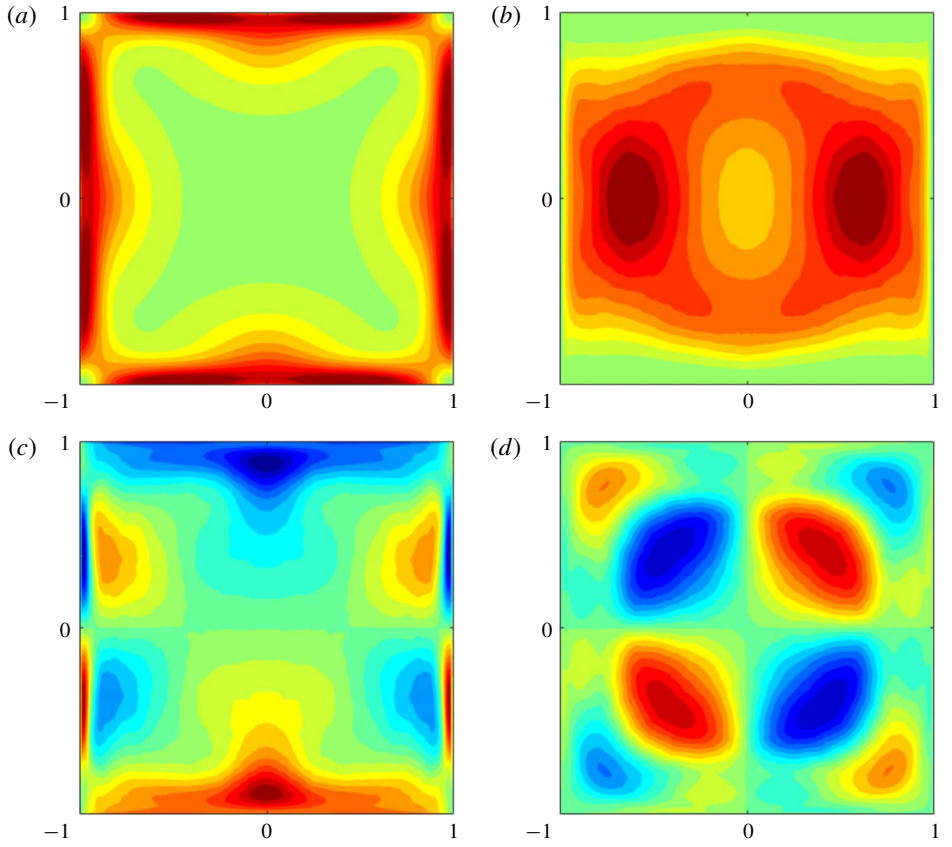


FIGURE 8. (Colour online) Contours of four components of the conformation tensor C_{ij}: (*a*) C_{11}, (*b*) C_{22}, (*c*) C_{12} and (*d*) C_{23}. Colour scales range from 30 (green) to 800 (red), from 5 (blue) to 50 (red), from −30 (blue) to 30 (red), and from −10 (blue) to 10 (red), for panels (*a*) to (*d*), respectively.

component C_{33} (not shown here). In particular, the in-plane diagonal component C_{22} is minimum at the wall, and acts mainly on the horizontal centreline. The cross-term C_{12} has its peak located at the walls, while the component C_{23} has its peaks on the two diagonals. The in-plane shear component C_{23} is not zero close to the corners, and over the two diagonals, where it shows a series of alternating maxima and minima, in a similar fashion to the shear Reynolds stress, which exhibits alternate signs moving from one wall to the other (figure 7). Figures 9(*a*), 9(*b*) and 9(*c*) show the wall-normal profiles of C_{11} (solid line) and $C_{22} + C_{33}$ (dashed line) in the midplane of the duct ($z = 0$), at $z = 0.3h$ and at $z = 0.6h$, respectively. Note that $C_{22} + C_{33}$ is a measure of the in-plane stretching of the polymers, while its sum with C_{11} is the trace of the conformation tensor. We observe that C_{11} (and the trace) has a peak close to the wall and then decreases to its minimum value in the centre of the duct. Also, the peak value increases moving from the midplane towards the sidewalls; C_{11} starts increasing for all $\tilde{y}$ close to the sidewalls ($z = 0.6h$) as we are approaching the sidewall peaks (see figure 8*a*). The in-plane stretching ($C_{22} + C_{33}$) is more moderate than the streamwise one, and the profiles show minimum values at the wall. Also, the peak values of $C_{22} + C_{33}$ are located around $h/2$ in the midplane

https://doi.org/10.1017/jfm.2018.858 Published online by Cambridge University Press

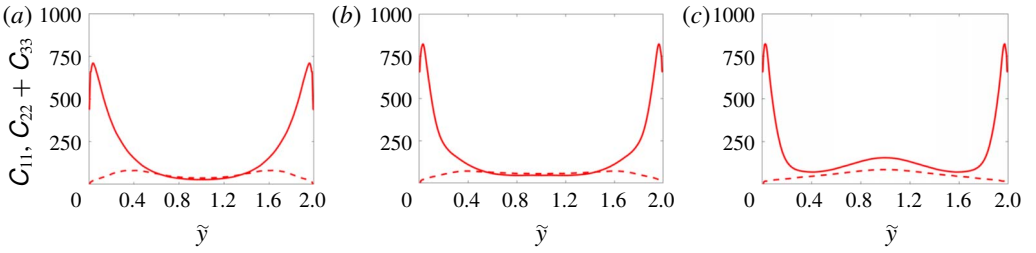


FIGURE 9. (Colour online) Mean profile of the streamwise C_{11} (solid line) and in-plane component $C_{22}+C_{33}$ (dashed line) of the conformation tensor C_{ij}. The panels correspond to different sections: (*a*) $z=0$, (*b*) $z=0.3h$ and (*c*) $z=0.6h$.

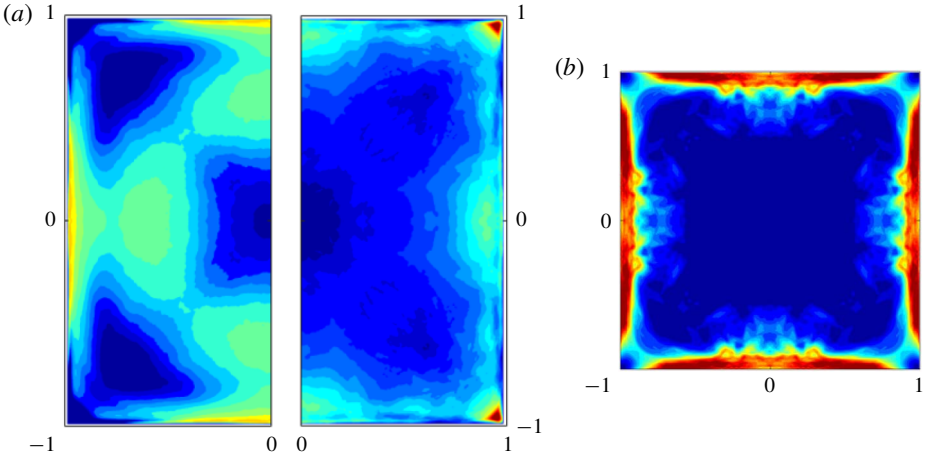


FIGURE 10. (Colour online) (*a*) Cross-correlations of the streamwise (left half) and wall-normal (right half) velocities and polymer force, defined in (3.1). Colour scales range from -1 to 1, and from -0.25 to 0.25, in the left and right halves, respectively. (*b*) Contours of the mean first normal difference $\mathcal{N}_1$, with the colour scale ranging from 0 (blue) to 0.35 (red).

and move towards $\tilde{y}=1$ when approaching the sidewalls (see figure 8*b*). Figures 8 and 9 show that the polymers mainly elongate in the streamwise direction in the near-wall region and away from the corners; however, in-plane elongation originating from the secondary cross-flow is present as well, especially at a distance from the walls of approximately $h/2$.

Next, figure 10(*a*) shows the cross-correlation ρ_i defined as

$$\rho_i = \frac{\overline{u_i f_i}}{u_{irms} f_{irms}}, \tag{3.1}$$

where f_i is the polymer volume force, i.e. the contribution to the Navier–Stokes equation of the polymeric stress tensor $f_i = (1-\beta)/Re\,\partial\tau_{ij}/\partial x_j$. The left half of figure 10(*a*) shows the streamwise component ρ_1, while the right half shows the two identical wall-normal ones $\rho_2=\rho_3$. In the streamwise direction (ρ_1), the polymer contribution is correlated with the corresponding velocity component in the near-wall

https://doi.org/10.1017/jfm.2018.858 Published online by Cambridge University Press

region of the midplane far from the corners, thus enhancing fluctuations in this particular region. On the contrary, the streamwise polymer body force and velocity become anticorrelated in the bulk of the flow away from the walls, where the polymer contribution opposes the turbulent fluctuations. This is similar to what was found by Dubief *et al.* (2005) for a turbulent plane channel flow. However, as the corners are approached, the behaviour drastically changes and the two streamwise components are strongly anticorrelated everywhere, even in the near-wall region, thus indicating that the addition of polymers tends to suppress fluctuation in the corners, as also shown in figure 7(*c*,*f*,*i*). The wall-normal component of the cross-correlation $\rho_{2,3}$ shows a different behaviour; the wall-normal velocity and polymer force are anticorrelated almost everywhere, especially in the bulk of the flow, while they are strongly correlated in the four corners, where the polymer in-plane stress is acting to enhance the turbulent fluctuations.

Finally, we analyse the mean first normal stress difference $\mathcal{N}_1 = \sigma_{11} - \sigma_{22}$, with σ_{11} and σ_{22} being the mean streamwise and wall-normal total stresses, i.e. the sum of the solvent and polymer stresses. The first normal stress difference $\mathcal{N}_1$ averaged over the whole domain is positive whereas the second one $\mathcal{N}_2$ is slightly negative, with $|\mathcal{N}_1/\mathcal{N}_2| \gg 1$. The spatial distribution of $\mathcal{N}_1$ is shown in figure 10(*b*); $\mathcal{N}_1$ is greater than zero in the whole domain and its peaks are located at the wall, around $0.5h$ from the sidewalls. Also, the first normal stress difference is close to zero at the centreline and in the four corners. Note that, as expected, the described spatial distribution of $\mathcal{N}_1$ closely follows that of C_{11} previously discussed in figure 8.

3.2. *Flow structures*

To further characterise the flow, we study the mean local wall stress along one edge in wall coordinates normalised by the average over the whole wall, similarly to what was proposed by Pinelli *et al.* (2010). These authors suggested that an upper bound for the number of wall velocity streaks over one of the four walls can be estimated from the dimension of the square expressed in wall units, since the average distance between streaks of different velocity sign is of the order of 50^+ (Kim *et al.* 1987). In our case, we can expect more streaks in the Newtonian case than in the viscoelastic flow with polymers since increasing streak spacing is a well-known effect of polymer drag reduction that has been observed in both experiment and numerical works (e.g. De Angelis, Casciola & Piva 2002). Indeed, this argument is confirmed by figure 11, which shows that in the Newtonian case each edge of the duct hosts up to five streaks, with two high-velocity streaks close to the sidewalls and one in the centre, and two low-velocity streaks in between, represented in figure 11 by the three maxima and two minima in the wall stress profile. In the drag-reduced case with polymers, the profile presents only two maxima and one minimum, indicating that two high-velocity streaks are close to the sidewalls and one low-velocity streak is located between them at the centre of the edge; also, the two peaks are closer to the centreline than in the Newtonian case. In figure 11, we also report with symbols three curves pertaining to the results by Pinelli *et al.* (2010) for a Newtonian duct flow at $Re_\tau = 178$ (▲), 150 (∗) and 120 (▼): the first is used as reference, showing the good agreement between our Newtonian results and those from the literature, while the other two are included to provide further insight into the polymeric flow. Indeed, the Newtonian case at $Re_\tau = 150$ has approximately the same Reynolds number as our polymeric flow (155), but still shows a local maximum at the centreline, while the Newtonian case at $Re_\tau = 120$ exhibits a pattern of minima and maxima similar to the one obtained by our

https://doi.org/10.1017/jfm.2018.858 Published online by Cambridge University Press

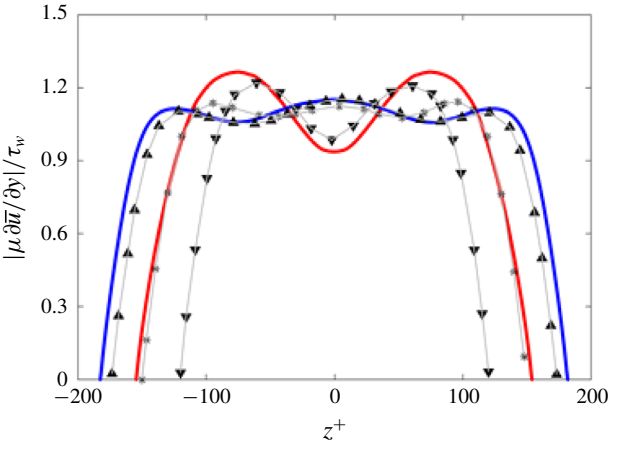


FIGURE 11. (Colour online) Mean local wall stress along one edge in wall coordinates normalised by the average over the whole wall τ_w. The blue and red lines are used to show our numerical results of the Newtonian and polymeric flows, respectively, while the grey lines with symbols are the data taken from the work of Pinelli *et al.* (2010) for three Newtonian flows with different Reynolds numbers: $Re_\tau = 178$ (▲), 150 (∗) and 120 (▼).

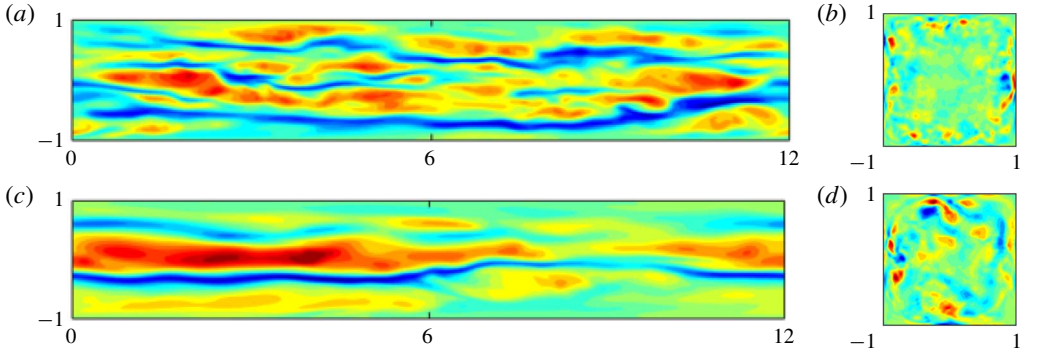


FIGURE 12. (Colour online) Contours of the instantaneous (*a*,*c*) streamwise velocity fluctuation component u' in the x–z plane located at $\widetilde{y} \approx 18^+$ from the wall and of (*b*,*d*) streamwise vorticity ω_x in the x–y plane. Panels show the Newtonian (*a*,*b*) and polymer (*c*,*d*) flows, respectively. The colour scale ranges from $-0.5U_b$ (blue) to $0.5U_b$ (red).

simulation with polymers, even if with different (lower) Reynolds number. Thus, even at a similar friction Reynolds number, the shear stress profile does not resemble that of a Newtonian flow due to the drag-reducing effect of polymers.

The previous result is confirmed by figure 12(*a*), which reports contours of the instantaneous streamwise velocity fluctuation u' in an x–z section located at a distance $\widetilde{y} \approx 18^+$ from one wall. Figure 12(*a*) clearly shows the instantaneous footprints of the near-wall low- and high-speed streaks. Even from an instantaneous picture of the flow, the difference between the Newtonian and polymeric flows appears evident; indeed, the former shows two long low-speed streaks and more than two high-speed streaks, which are shorter and wider than the low-speed ones, whereas the

https://doi.org/10.1017/jfm.2018.858 Published online by Cambridge University Press

viscoelastic flow presents just one low-speed streak close to the centreline, bounded by two high-speed streaks. Further, both the low- and high speed streaks are stronger and correlated over longer distances in the streamwise direction in the presence of polymers (Warholic *et al.* 1999; Escudier *et al.* 2009). Pinelli *et al.* (2010) showed that the mean streamwise vorticity (secondary flow) strongly depends upon the statistically preferred location of the quasi-streamwise vortices associated with the pair of fast/slow streaks closest to the corner. As just shown in figures 11 and 12, the inclusion of the polymers in the flow strongly modifies these structures, by enhancing the streamwise coherence of the flow and by increasing the size of the near-wall structures (see figure 12*c*), thus moving the quasi-streamwise vortices away from the bottom wall and sidewalls: therefore, the secondary motion is characterised by large structures close to the centre of the duct, due to the constraint imposed by the size of the domain.

3.3. *Vorticity budget*

Gavrilakis (1992) explains the origins of the mean secondary flow using an equation for the mean streamwise vorticity $\overline{\omega}_x$, which we here modify for a fully developed duct flow with polymers and whose derivation has been reported in appendix A. The equation for the streamwise vorticity reads

$$\frac{\partial \overline{\omega}_x}{\partial t} = \underbrace{\overline{v}\frac{\partial \overline{\omega}_x}{\partial y} + \overline{w}\frac{\partial \overline{\omega}_x}{\partial z}}_{\mathcal{C}} + \underbrace{\frac{\partial^2}{\partial y \partial z}(\overline{w'w'} - \overline{v'v'})}_{\mathcal{A}} + \underbrace{\left(\frac{\partial^2}{\partial y^2} - \frac{\partial^2}{\partial z^2}\right)\overline{v'w'}}_{\mathcal{D}}$$
$$\underbrace{-\frac{\beta}{Re}\left(\frac{\partial^2}{\partial y^2} + \frac{\partial^2}{\partial z^2}\right)\overline{\omega}_x}_{\mathcal{V}} \underbrace{-\frac{1-\beta}{Re}\left(\frac{\partial^2 \overline{\tau}_{32}}{\partial y^2} + \frac{\partial^2 \overline{\tau}_{33}}{\partial z \partial y} - \frac{\partial^2 \overline{\tau}_{22}}{\partial y \partial z} - \frac{\partial^2 \overline{\tau}_{23}}{\partial z^2}\right)}_{\mathcal{P}} = 0. \tag{3.2}$$

The first two terms in the equation (denoted as $\mathcal{C}$) are the convection of the mean vorticity by the secondary flow itself, while the last two terms are a sink of streamwise vorticity due to the viscosity ($\mathcal{V}$) and the polymer contribution ($\mathcal{P}$), which we found to be a sink as well. The two remaining terms involve the Reynolds stresses: the first is a production term associated with the anisotropy of the in-plane normal stresses ($\mathcal{A}$), while the second ($\mathcal{D}$) can be both a production and dissipation term due to the cross-Reynolds-stress component $\overline{v'w'}$. Figure 13 shows the contribution of the five terms highlighted in (3.2), i.e. $\mathcal{C}$, $\mathcal{A}$, $\mathcal{D}$, $\mathcal{V}$ and $\mathcal{P}$, in one of the eight sectors and averaged among all the sectors. Blue and red colours are used for the Newtonian and polymeric flows, respectively. The only positive contribution in the Newtonian case is provided by the anisotropic terms, while all the others are negative. With polymers, the polymeric contribution $\mathcal{P}$ is found to be a sink of vorticity, the anisotropic and viscous terms decrease in magnitude compared to the Newtonian flow, while $\mathcal{D}$ changes sign and increases in magnitude, changing from dissipation for the Newtonian flow to production for the flow with polymers. Finally, the convection term $\mathcal{C}$ is null for both cases. The budget analysis suggests that, although the polymeric stress is small in amplitude, its presence modifies the flow itself, by reducing the anisotropy of the in-plane velocity fluctuations.

3.4. *Energy budget*

To better understand the effect of polymers on the streamwise velocity fluctuations $\overline{u'u'}$, which are related to streaks, we consider the perturbation energy budget. The

https://doi.org/10.1017/jfm.2018.858 Published online by Cambridge University Press

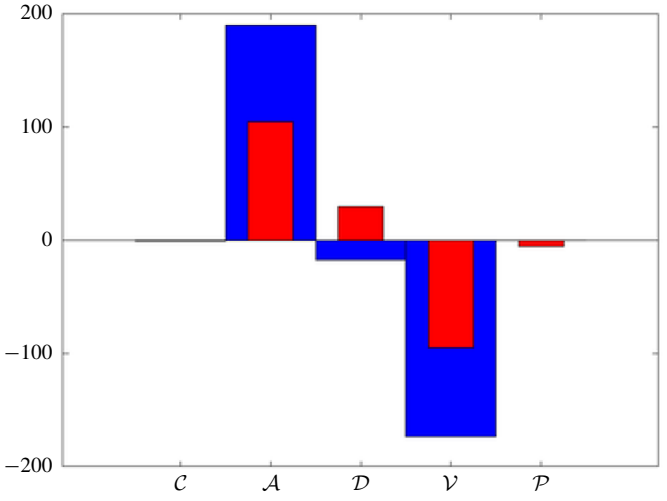


FIGURE 13. (Colour online) Contributions to the budget of the mean streamwise vorticity $\overline{\omega}_x$: convection $\mathcal{C}$, production due to anisotropy of the Reynolds stress $\mathcal{A}$, production/dissipation source term $\mathcal{D}$, viscous dissipation $\mathcal{V}$, and polymeric contribution $\mathcal{P}$. Blue and red colours are used for the Newtonian and viscoelastic flows, respectively.

transport equation for the Reynolds stress in a viscoelastic flow is given by

$$\frac{\partial \overline{u_i' u_j'}}{\partial t} = \underbrace{-\overline{u}_k \frac{\partial \overline{u_i' u_j'}}{\partial x_k}}_{\mathcal{A}_{ij}} \underbrace{-\overline{u}_k \frac{\partial \overline{u_i' u_j' u_k'}}{\partial x_k}}_{\mathcal{Q}_{ij}} \underbrace{-\left(\overline{u_j' \frac{\partial p'}{\partial x_i}} + \overline{u_i' \frac{\partial p'}{\partial x_j}}\right)}_{\mathcal{R}_{ij}} \underbrace{-\left(\overline{u_j' u_k'} \frac{\partial \overline{u}_i}{\partial x_k} + \overline{u_i' u_k'} \frac{\partial \overline{u}_j}{\partial x_k}\right)}_{\mathcal{P}_{ij}}$$
$$+ \underbrace{\frac{\beta}{Re} \frac{\partial^2 \overline{u_i' u_j'}}{\partial x_k^2}}_{\mathcal{D}_{ij}} \underbrace{-\frac{2\beta}{Re} \overline{\frac{\partial u_i'}{\partial x_k} \frac{u_j'}{\partial x_k}}}_{\epsilon_{ij}} + \underbrace{\frac{1-\beta}{Re} \left(\overline{u_j' \frac{\partial \tau_{ik}'}{\partial x_k}} + \overline{u_i' \frac{\partial \tau_{jk}'}{\partial x_k}}\right)}_{\mathcal{W}_{ij}} = 0, \tag{3.3}$$

where $\mathcal{A}_{ij}$ is the advection by the mean flow, $\mathcal{Q}_{ij}$ the transport by the velocity fluctuations, $\mathcal{R}_{ij}$ the pressure term, $\mathcal{P}_{ij}$ the production against the mean shear, $\mathcal{D}_{ij}$ the viscous diffusion, ϵ_{ij} the dissipation, and $\mathcal{W}_{ij}$ the polymer work. The evolution equation for the perturbation energy is obtained by setting $i=j$, and in particular we consider here the streamwise component $i=j=1$. Figure 14 shows the contours of these seven contributions, and their sum, for the Newtonian (a,c) and polymeric flow (b,d). First, we note that, as expected, the sum of all the contribution is in both cases almost zero (up to 10^{-3}), since the mean Reynolds stress $\overline{u'u'}$ has reached steady state.

We first discuss the Newtonian flow, reported in figure 14(a,c); the advection $\mathcal{A}_{ij}$ and transport $\mathcal{Q}_{ij}$ terms display strong gradients close to the walls. In particular, the distribution of $\mathcal{A}_{ij}$ reveals that the maximum advection occurs in regions close to the maximum in-plane mean vorticity, i.e. where the secondary flow is maximum (see figure 4). On the other hand, the turbulent transport, $\mathcal{Q}_{ij}$, is observed to be approximately uniform along the edges; in particular, it is zero at the wall, reaches a positive peak value in the near-wall region, followed by a minimum, and finally goes back to zero away from the wall, thus indicating that the largest gradients of the

https://doi.org/10.1017/jfm.2018.858 Published online by Cambridge University Press

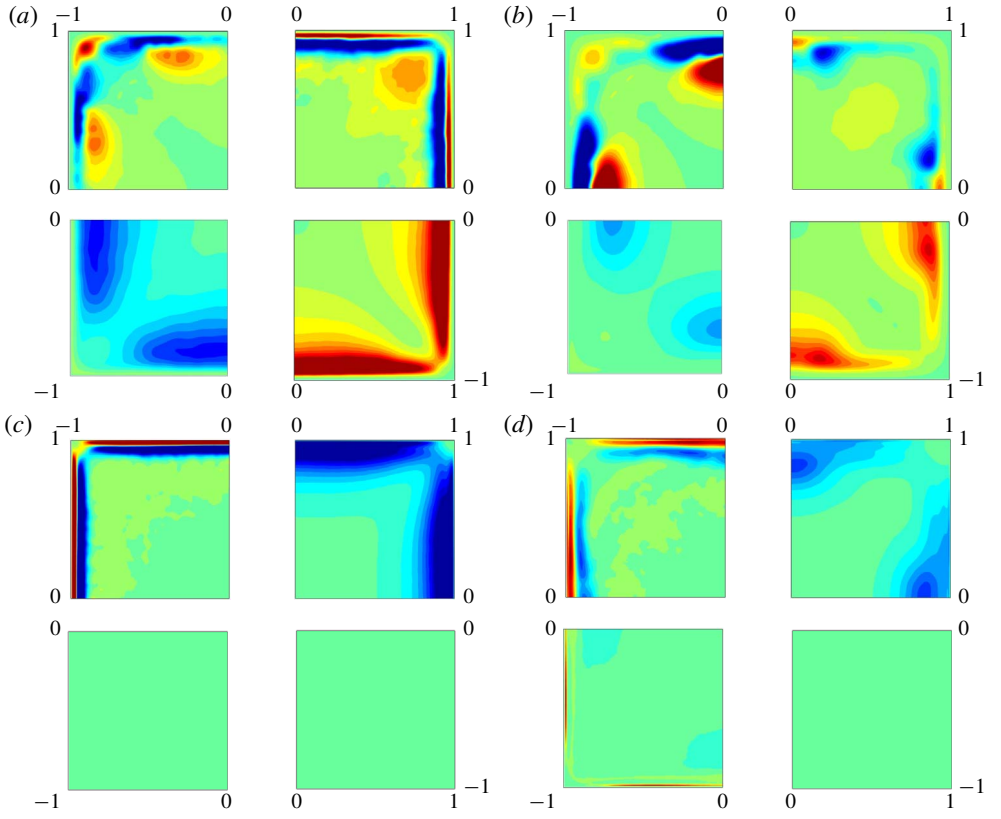


FIGURE 14. (Colour online) Contributions to the streamwise Reynolds-stress tensor $\overline{u'u'}$ equation for the Newtonian (*a*,*c*) and viscoelastic case with polymers (*b*,*d*). On each side (*a*,*c*) and (*b*,*d*), the contours represent the terms $\mathcal{A}_{ij}$, $\mathcal{Q}_{ij}$, $\mathcal{R}_{ij}$, $\mathcal{P}_{ij}$, $\mathcal{D}_{ij}$, ϵ_{ij}, $\mathcal{W}_{ij}$ and the total balance (see (3.3)) in order from top left to bottom right. The ranges of the colour scales are ± 0.002, ± 0.008, ± 0.005, ± 0.025, ± 0.01, ± 0.02, ± 0.003 and ± 0.001, respectively, from top left to bottom right, with colours going from blue (negative values) to red (positive value) and with the zero coloured in green.

high-order statistics are located mainly in the near-wall region, all along the edges. The pressure and production terms, $\mathcal{R}_{ij}$ and $\mathcal{P}_{ij}$, exhibit opposite behaviour: the former is always negative and the latter always positive, reaching a minimum/maximum and then approaching zero again in the bulk of the duct. The viscous diffusion $\mathcal{D}_{ij}$ displays a strong peak at the wall and then decreases to zero, while the dissipation term ϵ_{ij} has a minimum at the wall, and then increases to its maximum value in the centre of the duct. Figure 14(*a*,*c*) shows that all the contributions have an almost uniform distribution along the edges, with only a weak dependence on the distance from the corners, except for the advection $\mathcal{A}_{ij}$ and transport $\mathcal{Q}_{ij}$ terms.

The behaviour of the various terms in the kinetic energy budget is different for the viscoelastic flow, as shown in figure 14(*b*,*d*). In this case, all the terms are not uniform along the edge and strongly depend on the distance from the sidewalls; this is related to the reduced friction Reynolds number of the flow and the consequent increase in size of the near-wall structures previously discussed. In particular, the positive and negative peaks of the advection $\mathcal{A}_{ij}$ term are found close to the centreline far

https://doi.org/10.1017/jfm.2018.858 Published online by Cambridge University Press

Case	Re	Wi	β	L^2	DR (%)
P	2800	1.5	0.90	3600	29
P-$Wi\uparrow$	2800	3.0	0.90	3600	43
P-$L\downarrow$	2800	1.5	0.90	900	27
P-$L\uparrow$	2800	1.5	0.90	5625	29
P-$\beta\uparrow$	2800	1.5	0.95	3600	25

TABLE 1. Summary of all the DNS performed at a fixed bulk Reynolds number equal to $Re = 2800$ and with different viscoelastic fluids.

from the corners, similarly to the transport term $\mathcal{Q}_{ij}$, which exhibits strong negative and positive peaks in the same region. Also, the pressure $\mathcal{R}_{ij}$, production $\mathcal{P}_{ij}$ and dissipation ϵ_{ij} terms exhibit a similar trend, with maxima and minima located away from the corner. Finally, the polymer contribution ($\mathcal{W}_{ij}$) is not null, but its amplitude is small compared to the other terms, and its distribution across the whole duct is almost uniform. These results clearly indicate that the polymers strongly modify the flow; in particular, their presence induces a less uniform flow in the duct, with most of the streamwise flow fluctuations displaced towards the centreline and away from the corner, as we have already noticed in figure 10. The location where on average the low- and high-speed streaks are present, as previously shown in figures 11 and 12, coincides with the location of major activity of the flow where strong peaks of advection, transport, production and dissipation are present.

3.5. *Elasticity effect*

We now assess the effect of the parameters defining the viscoelastic behaviour of the fluid. Table 1 reports all the different simulations that we have performed and the drag reduction DR obtained in each case. In particular, starting from the reference polymeric case discussed before (P), we have varied independently the Weissenberg number Wi (P-$Wi\uparrow$), the dumbbell extensibility L (P-$L\downarrow$ and P-$L\uparrow$) and the viscosity ratio β (P-$\beta\uparrow$). From table 1 we can observe that, starting from the drag reduction reported for the reference polymeric case (29 %), a relevant reduction or increase of L brings about only small variations in the overall drag reduction (27 % and 29 %), while even smaller variations of β are sufficient to alter the solution, as demonstrated by a drag reduction of 25 % for the case with higher viscosity ratio P-$\beta\uparrow$. However, the parameter that has the greatest effect on the solution appears to be the Weissenberg number Wi. Indeed, when $Wi = 3$ (P-$Wi\uparrow$) the drag reduction increases to 43 %. We will now analyse in more detail this polymeric case with $Wi = 3$ and compare the flow with the one discussed above, i.e. the Newtonian and the polymeric with $Wi = 1.5$.

Figure 15 shows the contours of the mean streamwise components of the velocity $\overline{u}$ and vorticity $\overline{\omega}_x$ for the two different Weissenberg numbers considered. As Wi increases, the maximum streamwise velocity is only slightly affected, while the maximum vorticity strongly decreases by 40 %. However, the integral of the vorticity keeps increasing, thus confirming a progressive increase of the in-plane motion with the Weissenberg number Wi. The location of maximum vorticity, marked with a black dot in figure 15, moves further away from the walls, displacing towards the centre; however, this displacement is smaller than what was previously observed when comparing the Newtonian case with the polymeric one with $Wi = 1.5$ (see figure 4*b*), thus indicating a nonlinear trend with Wi.

https://doi.org/10.1017/jfm.2018.858 Published online by Cambridge University Press

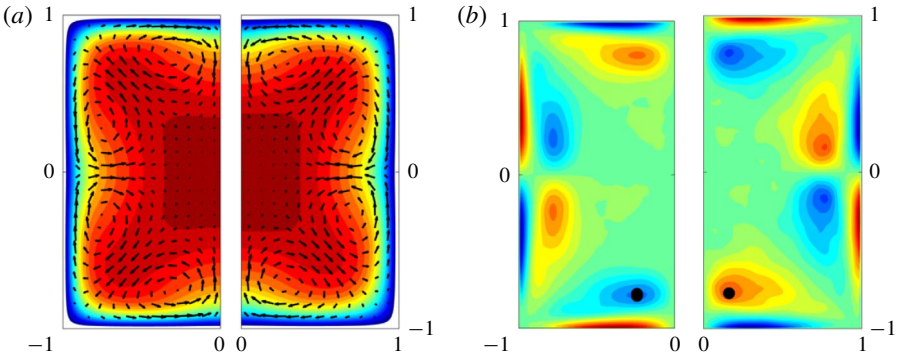


FIGURE 15. (Colour online) Contours of the mean streamwise component of (*a*) velocity $\overline{u}$ and (*b*) vorticity $\overline{\omega}_x$. In each panel, the left (right) half of the duct is used for the polymeric cases with $Wi = 1.5$ ($Wi = 3$), respectively. The colour scale ranges from 0 (blue) to $1.4U_b$ (red) in (*a*), and from $-0.5U_b/h$ (blue) to $0.5U_b/h$ (red) in (*b*). Panel (*a*) also reports the in-plane mean velocity with arrows.

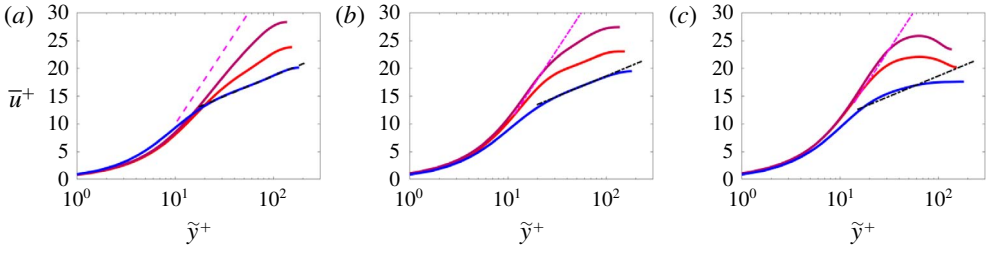


FIGURE 16. (Colour online) Mean streamwise velocity as a function of the wall-normal distance in logarithmic scale and wall units. The blue, red and brown lines are used for the numerical results without and with polymers with $Wi = 1.5$ and 3, respectively. The magenta dashed line is the polymer maximum drag reduction (Virk 1975; Lvov *et al.* 2004) while the black dashed line indicates the Newtonian log law. The panels correspond to different sections: (*a*) $z = 0$, (*b*) $z = 0.3h$ and (*c*) $z = 0.6h$.

Next, we study the mean streamwise velocity profiles in wall units reported in figure 16. Here, we compare the profiles of the Newtonian fluid and the two viscoelastic cases with different Weissenberg number *Wi*. In all the considered sections, we observe a progressive departure from the Newtonian velocity profile as *Wi* increases, with the slope of the inertial range of scales growing with *Wi*; the curves for $Wi = 3$ approach the maximum drag reduction limit.

Figure 17 shows the profiles of the r.m.s. of the velocity fluctuations and of the Reynolds shear stress component as a function of the wall-normal distance $\tilde{y}$. We observe that the streamwise velocity fluctuation u_{rms} is only slightly altered by the increase of *Wi*, except its peak value, which displaces further away from the wall. On the other hand, both the in-plane fluctuation v_{rms} and the shear Reynolds stress component $\overline{u'v'}$ are strongly affected by the increase of *Wi*. In particular, both v_{rms} and $\overline{u'v'}$ are reduced across the whole domain, as already found for the turbulent channel flows with polymers (Ptasinski *et al.* 2003; Dubief *et al.* 2004).

Finally, we report in figure 18 the effect of the Weissenberg number on the mean first normal stress difference $\mathcal{N}_1$. This strongly increases with *Wi*, with its

https://doi.org/10.1017/jfm.2018.858 Published online by Cambridge University Press

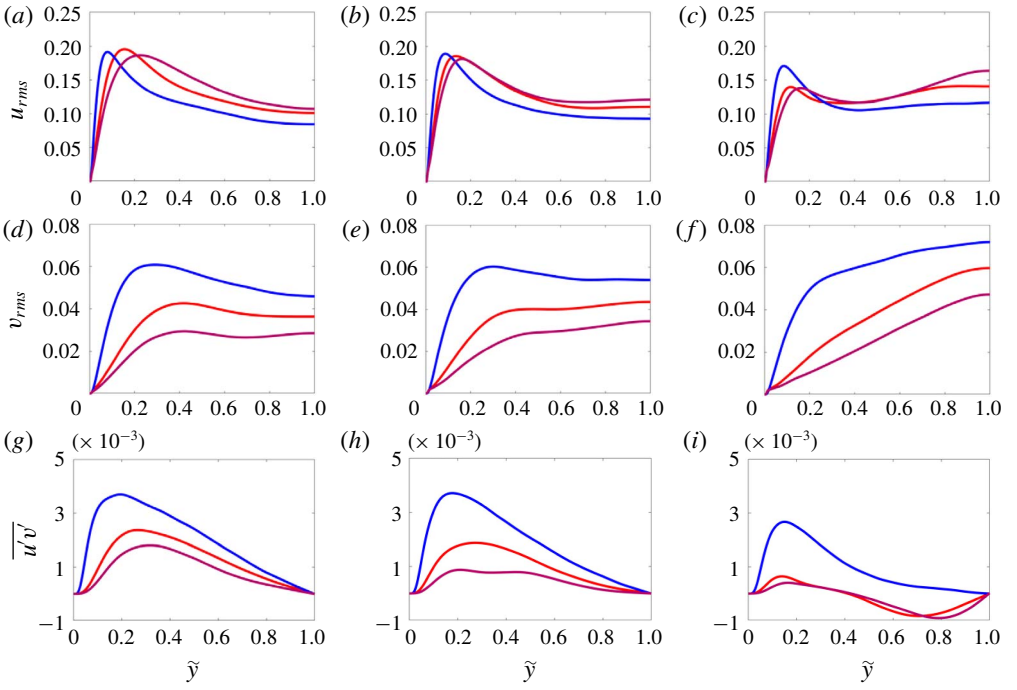


FIGURE 17. (Colour online) Wall-normal mean profile of (*a–c*) the streamwise r.m.s. velocity fluctuation, (*d–f*) the wall-normal r.m.s. velocity fluctuation, and (*g–i*) the cross-term of the Reynolds stress tensor $u'v'$. The columns correspond to different sections: (*a*,*d*,*g*) $z = 0$, (*b*,*e*,*h*) $z = 0.3h$ and (*c*,*f*,*i*) $z = 0.6h$. The line and colour style is the same as in figure 16.

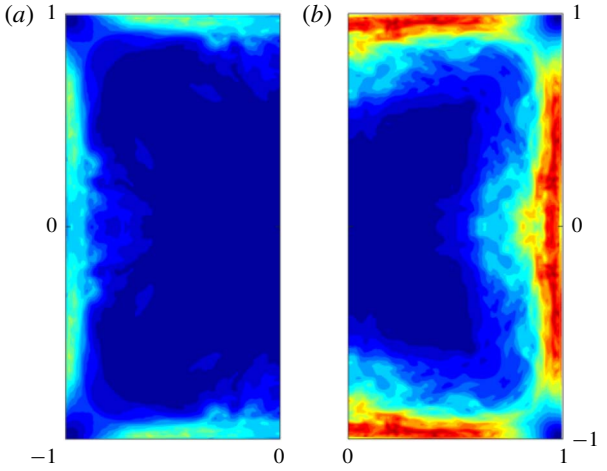


FIGURE 18. (Colour online) Contours of the mean first normal difference $\mathcal{N}_1$, with the colour scales ranging from 0 (blue) to 0.8 (red) for the polymeric cases with $Wi = 1.5$ (*a*) and $Wi = 3$ (*b*).

https://doi.org/10.1017/jfm.2018.858 Published online by Cambridge University Press

maximum value growing from approximately 0.3 for $Wi = 1.5$ (figure 18*a*) to 0.8 in the high-Weissenberg-number case (figure 18*b*). We also note that the spatial distribution remains similar for the different Wi studied here, with the peak values of $\mathcal{N}_1$ close to the walls and decreasing to almost zero in the centre of the duct and in the four corners. However, while for $Wi = 1.5$ the region close to the centreline showed small values of the first normal stress difference, with a peak located at a distance of approximately $0.5h$ from the sidewalls, the case with $Wi = 3$ exhibits a more uniform distribution around the wall bisectors, except in the corners, where it remains almost zero.

4. Conclusion

We have performed numerical simulations of a turbulent duct flow with polymers, and compared the results with those of a Newtonian flow. The numerical simulations are direct numerical simulations, where all the space and time scales of the flow are resolved, and the presence of polymers is modelled with the FENE-P closure. The numerical simulations are performed at a fixed moderate Reynolds number $Re = 2800$, resulting in a friction Reynolds number of 185 for the Newtonian flow and 155 for the viscoelastic counterpart with $Wi = 1.5$, $\beta = 0.9$ and $L^2 = 3600$; thus, the addition of polymers produces a drag reduction of approximately 30 % at the chosen Reynolds number. How the drag reduction is obtained and how it affects the secondary flow present in turbulent duct flows have been examined by various analyses.

We show that the mean streamwise velocity component is larger close to the corners in the viscoelastic flow than in the Newtonian case; the secondary flow is modified, with the locations of the maximum vorticity moving towards the centre, away from the walls, and an increase of the circulation in each of the eight sectors. These effects are observed in the presence of polymers that strongly modifies the quasi-streamwise vortices and the low- and high-speed streaks; in particular, their streamwise coherence is enhanced, they grow in size and depart from the walls, as already documented for turbulent plane channel flows with polymers. It is observed that, on average, each edge hosts up to two high-speed streaks and one low-speed one, similarly to what is found in duct flows at much lower bulk Reynolds number than the one considered here. However, we also found the flow to be deeply different from a Newtonian flow at the same friction Reynolds number.

The change in the near-wall turbulent structures is accompanied by a modification of the turbulent fluctuations and stresses: the streamwise velocity fluctuations increase in the polymeric flow, whereas the in-plane components and the shear stresses are strongly reduced. In particular, it is found that the polymer force tends to reduce streamwise turbulent fluctuations in the bulk of the flow and in the four corners, while promoting those close to the walls, whereas the wall-normal fluctuations are always reduced except in the corners. This is further discussed in connection with the mean streamwise vorticity budget, related to the cross-flow velocity. The analysis reveals that, although the polymeric contribution has a very small amplitude, the presence of polymers in the flow produces macroscopic changes in the flow itself; in particular, the contribution related to the in-plane derivatives of $\overline{v'w'}$ changes sign and becomes a production term, rather than a sink for the secondary motion.

The streamwise perturbation energy budget is also used to discuss the flow modification in the presence of polymers: again, we show that the viscoelastic flow is less uniform than its Newtonian counterpart, with the streamwise turbulent activity displaced farther away from the corners, towards the centreline. Also, the direct

https://doi.org/10.1017/jfm.2018.858 Published online by Cambridge University Press

contribution of the polymer stress term in the energy budget is small in amplitude, but the polymer addition substantially modifies the flow itself, as for the streamwise vorticity budget.

We investigate the effect of the different parameters defining the viscoelastic behaviour of the fluid, and show that the solution significantly changes with *Wi*. As the Weissenberg number is increased, the cross-stream vortical structures keep increasing in size, with their centre further away from the wall. The slope of the inertial range strongly increases with *Wi* and the mean velocity profile approaches the maximum drag reduction asymptote. All the in-plane velocity fluctuations are strongly reduced by an increase of *Wi*, except for the streamwise component, which on the contrary remains almost unaltered.

Acknowledgements

This work was supported by the European Research Council grant no. ERC-2013-CoG-616186, TRITOS and by the Swedish Research Council grant no. VR 2014-5001. The authors acknowledge computer time provided by SNIC (Swedish National Infrastructure for Computing).

Appendix A. Derivation of the vorticity budget

In this appendix we derive the equation for the mean streamwise vorticity component $\overline{\omega}_x$,

$$\overline{\omega}_x = \frac{\partial \overline{w}}{\partial y} - \frac{\partial \overline{v}}{\partial z}. \tag{A 1}$$

Using the Reynolds decomposition, the instantaneous flow variables are written as the sum of their mean value and fluctuation, i.e.

$$u_i = \overline{U}_i + u_i', \quad p = \overline{p} + p', \quad \tau_{ij} = \overline{\tau}_{ij} + \tau_{ij}', \tag{A 2a–c}$$

so as to obtain the following mean momentum equation:

$$\frac{\partial \overline{u}_i \overline{u}_j}{\partial x_j} + \frac{\partial \overline{u_i' u_j'}}{\partial x_j} = -\frac{\partial \overline{p}}{\partial x_i} + \frac{\beta}{Re}\frac{\partial^2 \overline{u}_i}{\partial x_j \partial x_j} + \frac{1-\beta}{Re}\frac{\partial \overline{\tau}_{ij}}{\partial x_j}, \tag{A 3}$$

where we have considered that the mean flow is stationary. The streamwise component of the curl of (A 3) then reads

$$\begin{aligned} &\frac{\partial}{\partial y}\left(\frac{\partial \overline{w}\,\overline{u}_j}{\partial x_j} + \frac{\partial \overline{w' u_j'}}{\partial x_j}\right) - \frac{\partial}{\partial z}\left(\frac{\partial \overline{v}\;\overline{u}_j}{\partial x_j} + \frac{\partial \overline{v' u_j'}}{\partial x_j}\right) \\ &\quad = \frac{\beta}{Re}\frac{\partial^2}{\partial x_j \partial x_j}\left(\frac{\partial \overline{w}}{\partial y} - \frac{\partial \overline{v}}{\partial z}\right) + \frac{1-\beta}{Re}\left(\frac{\partial^2 \overline{\tau}_{3j}}{\partial x_j \partial y} - \frac{\partial^2 \overline{\tau}_{2j}}{\partial x_j \partial z}\right). \end{aligned} \tag{A 4}$$

Note that Schwarz's theorem has been used. By using the definition of streamwise vorticity (A 1), the homogeneity in the streamwise x-direction ($\partial/\partial x = 0$), and the incompressibility constraint for the mean flow ($\partial \overline{v}/\partial y + \partial \overline{w}/\partial z = 0$), one can write

$$\begin{aligned} &\overline{v}\frac{\partial \overline{\omega}_x}{\partial y} + \overline{w}\frac{\partial \overline{\omega}_x}{\partial z} + \frac{\partial}{\partial y}\left(\frac{\partial \overline{w'v'}}{\partial y} + \frac{\partial \overline{w'w'}}{\partial z}\right) - \frac{\partial}{\partial z}\left(\frac{\partial \overline{v'v'}}{\partial y} + \frac{\partial \overline{v'w'}}{\partial z}\right) \\ &\quad = \frac{\beta}{Re}\left(\frac{\partial^2}{\partial y^2} + \frac{\partial^2}{\partial z^2}\right)\overline{\omega}_x + \frac{1-\beta}{Re}\left(\frac{\partial^2 \overline{\tau}_{32}}{\partial y^2} + \frac{\partial^2 \overline{\tau}_{33}}{\partial z \partial y} - \frac{\partial^2 \overline{\tau}_{22}}{\partial y \partial z} - \frac{\partial^2 \overline{\tau}_{23}}{\partial z^2}\right). \end{aligned} \tag{A 5}$$

https://doi.org/10.1017/jfm.2018.858 Published online by Cambridge University Press

Finally, the equation can be rearranged to obtain (3.2):

$$\overline{v}\frac{\partial\overline{\omega}_x}{\partial y}+\overline{w}\frac{\partial\overline{\omega}_x}{\partial z}+\frac{\partial^2}{\partial y\partial z}\left(\overline{w'w'}-\overline{v'v'}\right)+\left(\frac{\partial^2}{\partial y^2}-\frac{\partial^2}{\partial z^2}\right)\overline{v'w'}$$
$$=\frac{\beta}{Re}\left(\frac{\partial^2}{\partial y^2}+\frac{\partial^2}{\partial z^2}\right)\overline{\omega}_x+\frac{1-\beta}{Re}\left(\frac{\partial^2\overline{\tau}_{32}}{\partial y^2}+\frac{\partial^2\overline{\tau}_{33}}{\partial z\partial y}-\frac{\partial^2\overline{\tau}_{22}}{\partial y\partial z}-\frac{\partial^2\overline{\tau}_{23}}{\partial z^2}\right). \quad (A\,6)$$

REFERENCES

ALVES, M. A., PINHO, F. T. & OLIVEIRA, P. J. 2000 Effect of a high-resolution differencing scheme on finite-volume predictions of viscoelastic flows. *J. Non-Newtonian Fluid Mech.* **93** (2), 287–314.

BIANCOFIORE, L., BRANDT, L. & ZAKI, T. A. 2017 Streak instability in viscoelastic Couette flow. *Phys. Rev. Fluids* **2** (4), 043304.

BREUGEM, W. P., BOERSMA, B. J. & UITTENBOGAARD, R. E. 2006 The influence of wall permeability on turbulent channel flow. *J. Fluid Mech.* **562**, 35–72.

BRUNDRETT, E. & BAINES, W. D. 1964 The production and diffusion of vorticity in duct flow. *J. Fluid Mech.* **19** (3), 375–394.

CHO, Y. I. & HARNETT, J. P. 1982 Non-Newtonian fluids in circular pipe flow. *Adv. Heat Transfer* **15**, 59–141.

CHOI, H., MOIN, P. & KIM, J. 1993 Direct numerical simulation of turbulent flow over riblets. *J. Fluid Mech.* **255**, 503–539.

DE ANGELIS, E., CASCIOLA, C. M. & PIVA, R. 2002 DNS of wall turbulence: dilute polymers and self-sustaining mechanisms. *Comput. Fluids* **31** (4), 495–507.

DE VITA, F., ROSTI, M. E., IZBASSAROV, D., DUFFO, L., TAMMISOLA, O., HORMOZI, S. & BRANDT, L. 2018 Elastoviscoplastic flow in porous media. *J. Non-Newtonian Fluid Mech.* **258**, 10–21.

DEALY, J. M. 2010 Weissenberg and Deborah numbers – their definition and use. *Rheol. Bull.* **79** (2), 14–18.

DEN TOONDER, J. M. J., HULSEN, M. A., KUIKEN, G. D. C. & NIEUWSTADT, F. T. M. 1997 Drag reduction by polymer additives in a turbulent pipe flow: numerical and laboratory experiments. *J. Fluid Mech.* **337**, 193–231.

DIMITROPOULOS, C. D., SURESHKUMAR, R., BERIS, A. N. & HANDLER, R. A. 2001 Budgets of Reynolds stress, kinetic energy and streamwise enstrophy in viscoelastic turbulent channel flow. *Phys. Fluids* **13** (4), 1016–1027.

DUBIEF, Y., TERRAPON, V. E., WHITE, C. M., SHAQFEH, E. S. G., MOIN, P. & LELE, S. K. 2005 New answers on the interaction between polymers and vortices in turbulent flows. *Flow Turbul. Combust.* **74** (4), 311–329.

DUBIEF, Y., WHITE, C. M., TERRAPON, V. E., SHAQFEH, E. S. G., MOIN, P. & LELE, S. K. 2004 On the coherent drag-reducing and turbulence-enhancing behaviour of polymers in wall flows. *J. Fluid Mech.* **514**, 271–280.

DUPRET, F. & MARCHAL, J. M. 1986 Loss of evolution in the flow of viscoelastic fluids. *J. Non-Newtonian Fluid Mech.* **20**, 143–171.

ESCUDIER, M. P., NICKSON, A. K. & POOLE, R. J. 2009 Turbulent flow of viscoelastic shear-thinning liquids through a rectangular duct: quantification of turbulence anisotropy. *J. Non-Newtonian Fluid Mech.* **160** (1), 2–10.

ESCUDIER, M. P., PRESTI, F. & SMITH, S. 1999 Drag reduction in the turbulent pipe flow of polymers. *J. Non-Newtonian Fluid Mech.* **81** (3), 197–213.

ESCUDIER, P. & SMITH, S. 2001 Fully developed turbulent flow of non-Newtonian liquids through a square duct. *Proc. R. Soc. Lond.* A **457**, 911–936.

GAMPERT, B., BRAEMER, T., EICH, T. & DIETMANN, T. 2005 Rheo-optical investigations and near-wall turbulence structure of polymer solutions in turbulent channel flow. *J. Non-Newtonian Fluid Mech.* **126** (2), 115–121.

https://doi.org/10.1017/jfm.2018.858 Published online by Cambridge University Press

GAMPERT, B. & RENSCH, A. 1996 Polymer concentration and near wall turbulence structure of channel flow of polymer solutions. In *Proceedings of ASME Fluids Engineering Division Summer Meeting*, vol. 237, pp. 129–136. ASME.

GAMPERT, B. & YONG, C. K. 1990 The influence of polymer additives on the coherent structure of turbulent channel flow. In *Structure of Turbulence and Drag Reduction*, pp. 223–232. Springer.

GARCÍA-MAYORAL, R. & JIMÉNEZ, J. 2011 Hydrodynamic stability and breakdown of the viscous regime over riblets. *J. Fluid Mech.* **678**, 317–347.

GAVRILAKIS, S. 1992 Numerical simulation of low-Reynolds-number turbulent flow through a straight square duct. *J. Fluid Mech.* **244**, 101–129.

GESSNER, F. B. 1973 The origin of secondary flow in turbulent flow along a corner. *J. Fluid Mech.* **58** (1), 1–25.

IZBASSAROV, D., ROSTI, M. E., NIAZI ARDEKANI, M., SARABIAN, M., HORMOZI, S., BRANDT, L. & TAMMISOLA, O. 2018 Computational modeling of multiphase viscoelastic and elastoviscoplastic flows. *Intl J. Numer. Meth. Fluids*; (in press, https://doi.org/10.1002/fld.4678).

JIANG, G. S. & SHU, C. W. 1996 Efficient implementation of weighted ENO schemes. *J. Comput. Phys.* **126** (1), 202–228.

JIMENEZ, J. & MOIN, P. 1991 The minimal flow unit in near-wall turbulence. *J. Fluid Mech.* **225**, 213–240.

KIM, J. & MOIN, P. 1985 Application of a fractional-step method to incompressible Navier–Stokes equations. *J. Comput. Phys.* **59** (2), 308–323.

KIM, J., MOIN, P. & MOSER, R. 1987 Turbulence statistics in fully developed channel flow at low Reynolds number. *J. Fluid Mech.* **177**, 133–166.

LI, C. F., SURESHKUMAR, R. & KHOMAMI, B. 2006 Influence of rheological parameters on polymer induced turbulent drag reduction. *J. Non-Newtonian Fluid Mech.* **140** (1), 23–40.

LOGAN, S. E. 1972 Laser velocimeter measurement of Reynolds stress and turbulence in dilute polymer solutions. *AIAA J.* **10** (7), 962–964.

LVOV, V. S., POMYALOV, A., PROCACCIA, I. & TIBERKEVICH, V. 2004 Drag reduction by polymers in wall bounded turbulence. *Phys. Rev. Lett.* **92** (24), 244503.

MADABHUSHI, R. K. & VANKA, S. P. 1991 Large eddy simulation of turbulence-driven secondary flow in a square duct. *Phys. Fluids* A **3** (11), 2734–2745.

MELLING, A. & WHITELAW, J. H. 1976 Turbulent flow in a rectangular duct. *J. Fluid Mech.* **78** (2), 289–315.

MIN, T., CHOI, H. & YOO, J. Y. 2003*a* Maximum drag reduction in a turbulent channel flow by polymer additives. *J. Fluid Mech.* **492**, 91–100.

MIN, T., YOO, J. Y. & CHOI, H. 2001 Effect of spatial discretization schemes on numerical solutions of viscoelastic fluid flows. *J. Non-Newtonian Fluid Mech.* **100** (1), 27–47.

MIN, T., YOO, J. Y., CHOI, H. & JOSEPH, D. D. 2003*b* Drag reduction by polymer additives in a turbulent channel flow. *J. Fluid Mech.* **486**, 213–238.

MOMPEAN, G. & DEVILLE, M. 1997 Unsteady finite volume simulation of Oldroyd-B fluid through a three-dimensional planar contraction. *J. Non-Newtonian Fluid Mech.* **72** (2–3), 253–279.

NIKURADSE, J. 1926 Untersuchung über die geschwindigkeitsverteilung in turbulenten strömungen. PhD thesis, Gottingen.

ORLANDI, P. & LEONARDI, S. 2008 Direct numerical simulation of three-dimensional turbulent rough channels: parameterization and flow physics. *J. Fluid Mech.* **606**, 399–415.

OWOLABI, B. E., DENNIS, D. J. C. & POOLE, R. J. 2017 Turbulent drag reduction by polymer additives in parallel-shear flows. *J. Fluid Mech.* **827**, R4.

OWOLABI, B. E., POOLE, R. J. & DENNIS, D. J. C. 2016 Experiments on low-Reynolds-number turbulent flow through a square duct. *J. Fluid Mech.* **798**, 398–410.

PINELLI, A., UHLMANN, M., SEKIMOTO, A. & KAWAHARA, G. 2010 Reynolds number dependence of mean flow structure in square duct turbulence. *J. Fluid Mech.* **644**, 107–122.

POOLE, R. J. 2012 The Deborah and Weissenberg numbers. *Rheol. Bull.* **53**, 32–39.

PRANDTL, L. 1926 Uber die ausgebildete turbulenz. Verh. 2nd Intl Kong. für Tech. Mech., Zurich. English translation: *NACA Tech. Memo* 62, p. 435.

https://doi.org/10.1017/jfm.2018.858 Published online by Cambridge University Press

PTASINSKI, P. K., BOERSMA, B. J., NIEUWSTADT, F. T. M., HULSEN, M. A., VAN DEN BRULE, B. H. A. A. & HUNT, J. C. R. 2003 Turbulent channel flow near maximum drag reduction: simulations, experiments and mechanisms. *J. Fluid Mech.* **490**, 251–291.

RESENDE, P. R., ESCUDIER, M. P., PRESTI, F., PINHO, F. T. & CRUZ, D. O. A. 2006 Numerical predictions and measurements of Reynolds normal stresses in turbulent pipe flow of polymers. *Intl J. Heat Fluid Flow* **27** (2), 204–219.

ROSTI, M. E. & BRANDT, L. 2017 Numerical simulation of turbulent channel flow over a viscous hyper-elastic wall. *J. Fluid Mech.* **830**, 708–735.

ROSTI, M. E. & BRANDT, L. 2018 Suspensions of deformable particles in a Couette flow. *J. Non-Newtonian Fluid Mech.* **262** (C), 3–11.

ROSTI, M. E., BRANDT, L. & MITRA, D. 2018*a* Rheology of suspensions of viscoelastic spheres: deformability as an effective volume fraction. *Phys. Rev. Fluids* **3** (1), 012301(R).

ROSTI, M. E., BRANDT, L. & PINELLI, A. 2018*b* Turbulent channel flow over an anisotropic porous wall – drag increase and reduction. *J. Fluid Mech.* **842**, 381–394.

ROSTI, M. E., CORTELEZZI, L. & QUADRIO, M. 2015 Direct numerical simulation of turbulent channel flow over porous walls. *J. Fluid Mech.* **784**, 396–442.

ROSTI, M. E., IZBASSAROV, D., TAMMISOLA, O., HORMOZI, S. & BRANDT, L. 2018*c* Turbulent channel flow of an elastoviscoplastic fluid. *J. Fluid Mech.* **853**, 488–514.

RUDD, M. J. 1972 Velocity measurements made with a laser dopplermeter on the turbulent pipe flow of a dilute polymer solution. *J. Fluid Mech.* **51** (4), 673–685.

SAMANTA, A., VINUESA, R., LASHGARI, I., SCHLATTER, P. & BRANDT, L. 2015 Enhanced secondary motion of the turbulent flow through a porous square duct. *J. Fluid Mech.* **784**, 681–693.

SUGIYAMA, K., II, S., TAKEUCHI, S., TAKAGI, S. & MATSUMOTO, Y. 2011 A full Eulerian finite difference approach for solving fluid–structure coupling problems. *J. Comput. Phys.* **230** (3), 596–627.

SURESHKUMAR, R. & BERIS, A. N. 1995 Effect of artificial stress diffusivity on the stability of numerical calculations and the flow dynamics of time-dependent viscoelastic flows. *J. Non-Newtonian Fluid Mech.* **60** (1), 53–80.

UHLMANN, M., PINELLI, A., KAWAHARA, G. & SEKIMOTO, A. 2007 Marginally turbulent flow in a square duct. *J. Fluid Mech.* **588**, 153–162.

VINUESA, R., SCHLATTER, P. & NAGIB, H. M. 2015 On minimum aspect ratio for duct flow facilities and the role of side walls in generating secondary flows. *J. Turbul.* **16** (6), 588–606.

VIRK, P. S. 1971 Drag reduction in rough pipes. *J. Fluid Mech.* **45** (2), 225–246.

VIRK, P. S. 1975 Drag reduction fundamentals. *AIChE J.* **21** (4), 625–656.

VIRK, P. S., MERRILL, E. W., MICKLEY, H. S., SMITH, K. A. & MOLLO-CHRISTENSEN, E. L. 1967 The Toms phenomenon: turbulent pipe flow of dilute polymer solutions. *J. Fluid Mech.* **30** (2), 305–328.

VIRK, P. S., MICKLEY, H. S. & SMITH, K. A. 1970 The ultimate asymptote and mean flow structure in Toms' phenomenon. *Trans. ASME J. Appl. Mech.* **37** (2), 488–493.

WARHOLIC, M. D., MASSAH, H. & HANRATTY, T. J. 1999 Influence of drag-reducing polymers on turbulence: effects of Reynolds number, concentration and mixing. *Exp. Fluids* **27** (5), 461–472.

WHITE, C. M., SOMANDEPALLI, V. S. R. & MUNGAL, M. G. 2004 The turbulence structure of drag-reduced boundary layer flow. *Exp. Fluids* **36** (1), 62–69.

XI, L. & GRAHAM, M. D. 2010 Active and hibernating turbulence in minimal channel flow of Newtonian and polymeric fluids. *Phys. Rev. Lett.* **104** (21), 218301.

XI, L. & GRAHAM, M. D. 2012*a* Dynamics on the laminar–turbulent boundary and the origin of the maximum drag reduction asymptote. *Phys. Rev. Lett.* **108** (2), 028301.

XI, L. & GRAHAM, M. D. 2012*b* Intermittent dynamics of turbulence hibernation in Newtonian and viscoelastic minimal channel flows. *J. Fluid Mech.* **693**, 433–472.

https://doi.org/10.1017/jfm.2018.858 Published online by Cambridge University Press